

# Cation exchange modification of clinoptilolite –thermodynamic effects on adsorption separations of carbon dioxide, methane, and nitrogen

D.A. Kennedy, M. Mujčin, C. Abou-Zeid, F.H. Tezel\*

Department of Chemical and Biological Engineering, University of Ottawa 161 Louis Pasteur, CBY A412 Ottawa, ON, K1N 6N5, Canada



## ARTICLE INFO

**Keywords:**

Cation exchanged clinoptilolite  
Adsorption  
CO<sub>2</sub>  
N<sub>2</sub>  
CH<sub>4</sub>  
Gas separation

## ABSTRACT

This study details an experimental analysis of the thermodynamics of adsorption equilibrium behaviour of pure CO<sub>2</sub>, CH<sub>4</sub>, and N<sub>2</sub> gases on raw, Fe<sup>3+</sup>, Ca<sup>2+</sup>, and Cs<sup>+</sup> cation exchanged clinoptilolite. Equilibrium adsorption isotherms were experimentally determined for CO<sub>2</sub>, CH<sub>4</sub>, and N<sub>2</sub> at three different temperatures ranging from 303 K up to 363 K, at pressures up to 8.0 atm using the microgravimetric technique. Kinetic adsorption uptake data was measured at different temperatures for CH<sub>4</sub> and N<sub>2</sub> gases, and the results were compared for raw and Ca<sup>2+</sup> clinoptilolite. Heat of adsorption values were calculated for all three gases on the studied clinoptilolite samples using the chromatographic method. These results were compared to the isosteric adsorption enthalpies determined from the adsorption isotherms at different temperatures. The isosteric heat of adsorption was the highest for CO<sub>2</sub> followed by CH<sub>4</sub>, and N<sub>2</sub>. Temperature dependent Sips, Toth, and Dual-Site Langmuir isotherm models were fitted with experimental data and selectivity factor values were calculated for CO<sub>2</sub>/CH<sub>4</sub> and CH<sub>4</sub>/N<sub>2</sub> gas separations using the regressed isotherm models. Ca<sup>2+</sup> clinoptilolite shows the best potential for CO<sub>2</sub>/CH<sub>4</sub> separations due to its high selectivity. However, higher temperatures are needed in order to compensate for the slow kinetic behaviour. For CH<sub>4</sub>/N<sub>2</sub> separations, Fe<sup>3+</sup> clinoptilolite selectivity displays both high values and less variability compared to Cs<sup>+</sup> clinoptilolite over a broader range of temperatures and pressures.

## 1. Introduction

Natural gas currently represents almost one quarter of global energy consumption [1]. While long term predictions suggest that renewable energy will one day replace fossil derived resources, growing demand for natural gas is expected to result in a 30% increase in consumption through to 2030 [2]. This trend has been driven by increased consumer demand and improved economic viability of previously entrapped unconventional natural gas sources through advanced extraction techniques. While raw natural gas contains predominately CH<sub>4</sub> (80–95%), a number of different components including CO<sub>2</sub> (typically < 5%) and N<sub>2</sub> (typically < 10%) are also present in natural gas mixtures among many others [3]. Some of these additional gases would need to be removed depending on the local conditions of the natural gas field relative to gas composition and heating value regulatory standards. Inert gases such as N<sub>2</sub> are to be rejected from the bulk gas to increase the heating value of the natural gas fuel and to improve the compression efficiency by reducing the total gas volume. Additionally, CO<sub>2</sub> is to be removed as a means to prevent freezing and corrosion within the gas processing and delivery equipment.

### 1.1. CO<sub>2</sub> and N<sub>2</sub> removal from natural gas type mixtures

Conventionally, CO<sub>2</sub> removal from natural gas is achieved using aqueous amine absorption scrubbing, whereas excess N<sub>2</sub> is rejected using cryogenic distillation technologies [4]. These methods are capable of achieving high equilibrium selectivity, however they both have several process disadvantages [5]. Some concerns with respect to amine absorption include: environmental concerns resulting from fugitive amine emissions and operation issues regarding premature process equipment corrosion. Additionally, a large amount of energy is required to achieve solvent regeneration temperatures for CO<sub>2</sub> stripping and for cooling to liquefaction temperatures in the case of nitrogen rejection. Production of sub-quality natural gas from remote locations, unconventional sources, or degraded fields requiring enhanced production techniques such as N<sub>2</sub> gas injection puts additional strain on these separation methods [6]. This is because the per-volume gas processing efficiency decreases rapidly with lower capacity. Additional gas treatment costs are incurred based on the volume of CO<sub>2</sub> and N<sub>2</sub> gas to be removed from the natural gas mixture. These limitations facilitate the need to explore alternative processing technologies capable of reducing the CO<sub>2</sub> and N<sub>2</sub> volume in raw gas feed. Pressure swing adsorption

\* Corresponding author.

E-mail address: [handan.tezel@uottawa.ca](mailto:handan.tezel@uottawa.ca) (F.H. Tezel).

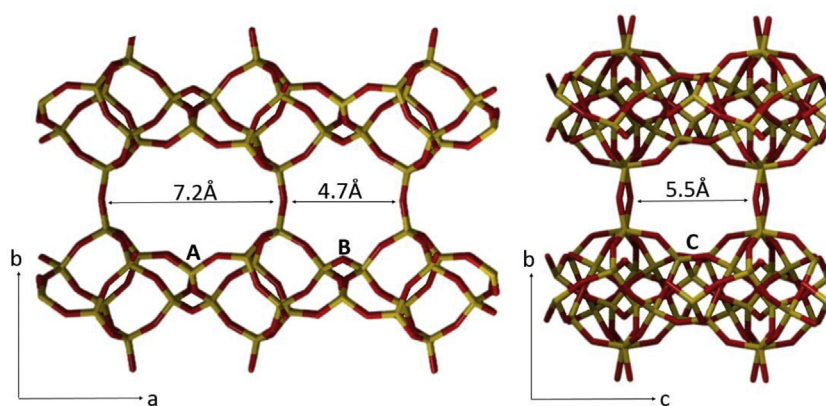


**Fig. 1.** The framework structure of clinoptilolite zeolite as described by the IZA, with the corresponding dimensions of the channel openings are shown [66,69,65]. The yellow sticks represent silicon or aluminum atoms and the red sticks represent the covalently shared oxygen atoms. (For interpretation of the references to colour in this figure legend, the reader is referred to the Web version of this article.)

(PSA) and Vacuum Swing Adsorption (VSA) are proposed as possible alternative solutions for separation of CO<sub>2</sub> and N<sub>2</sub> from natural gas type mixtures. These technologies are particularly attractive for smaller scale field processing volumes and for treating nitrogen-rich natural gas streams [7,8]. Additionally, sources of fugitive methane emissions from appreciably lower quality stocks including coal-bed gas, coal-mine ventilation gas, as well as biogas are also targets for CH<sub>4</sub> enrichment through PSA processes due to the high volume of contaminants CO<sub>2</sub> and/or N<sub>2</sub> gases. For a pressure swing adsorption process directed towards natural gas upgrading, there exists a desirability of having the CH<sub>4</sub> as the least adsorbed component so that it remains in the high pressure raffinate stream following the adsorption step. While not absolutely essential, this configuration reduces the mechanical work needed to re-pressurize the refined CH<sub>4</sub> gas.

### 1.1.1. Adsorbents for CO<sub>2</sub> removal from CH<sub>4</sub>

Several adsorbent materials have been proposed and screened for the separation CO<sub>2</sub> from CH<sub>4</sub> including various zeolite types [9–18], activated carbons [19–26], metal organic frameworks (MOFs) [27–34], and many others [5]. Enhanced CO<sub>2</sub> selectivity has been achieved using novel amine surface functionalized adsorbents [23,35–39]. However, thermally induced structural degradation and reactive deactivation of the supported amine in the presence of common natural gas contaminants has shown to effect the long term stability of these materials [40–42]. With respect to MOFs, while exceptional CO<sub>2</sub> adsorption capacities have been reported, the vulnerability of metal – ligand framework to moisture, and thermal degradation is well documented and has been the subject of several contributions [43–48]. Therefore, zeolites and activated carbons are still considered advantageous in this regard due to their better temperature and chemical stability. Kacem et al. directly screened and compared the function of various zeolites and activated carbons for the separation of CO<sub>2</sub>–CH<sub>4</sub> mixtures [49]. Generally, activated carbons exhibit higher CO<sub>2</sub> loadings at high pressures compared to zeolites (5A and 13X), whereas the zeolites showed higher CO<sub>2</sub>/CH<sub>4</sub> selectivity at low to moderate pressures, especially in the vacuum pressure region. Experimental cyclic PSA studies (T = 298 K, P = 1–30 atm) showed repeatable reversibility for both material types after 2–3 cycles, with CH<sub>4</sub> purity and recoveries being higher for zeolite 13X compared to activated carbon for an equimolar CO<sub>2</sub>–CH<sub>4</sub> gas feed mixture [49]. Similarly, Cavenati, et al. proposed a VPSA system (T = 299 K, P = 0.05–5 atm) which showed that CH<sub>4</sub> recoveries of greater than 80% were possible for a (60% CH<sub>4</sub> + 20% CO<sub>2</sub> + 20% N<sub>2</sub>) mixture, giving a CH<sub>4</sub> product purity of about 80%

using 13X zeolite [9]. To date, several successful commercial adsorption based applications for CO<sub>2</sub>/CH<sub>4</sub> separation have been implemented most involving the use of activated carbons or some other proprietary adsorbent material. A review conducted by Rufford et al. presents an excellent summary of these commercialized technologies [5].

### 1.1.2. Adsorbents for N<sub>2</sub> removal from CH<sub>4</sub>

In most cases, CH<sub>4</sub>/N<sub>2</sub> adsorption equilibrium selectivity is only moderate and typically ranges between 2.1 and 5.5 for activated carbons [50,51] and 1.3–1.7 for many zeolites [52,53] under standard conditions. However, CH<sub>4</sub> is larger than N<sub>2</sub> (kinetic diameter is 3.84 Å for CH<sub>4</sub> vs. 3.60 Å for N<sub>2</sub>), therefore microporous adsorbents with a similarly small pore size have also been explored for this separation. Small pored adsorbents compound the effect of steric limitations and have a favourable influence on inducing a desired N<sub>2</sub>/CH<sub>4</sub> gas separation. Microporous materials such as zeolite 4A [54], chabazite [54,55], mordenite [54,56], clinoptilolite [57–59], carbon molecular sieve [26,60–62] (CMS), and MOF [63] have all been studied in this regard. However, most are moderately CH<sub>4</sub> equilibrium selective, but have high N<sub>2</sub>/CH<sub>4</sub> kinetic selectivity. In some cases, equilibrium selectivity for CH<sub>4</sub> over N<sub>2</sub> can be reversed such that N<sub>2</sub> is the more adsorbed component. This is the case with titanosilicate ETS-4, whereby the pore size of this material may be tailored to achieve preferential adsorption of smaller gases such as N<sub>2</sub> over larger gases such as CH<sub>4</sub> or C<sub>2</sub>H<sub>6</sub> [64]. Guild Associates' Molecular Gate Adsorption Technology® remains the benchmark for commercial N<sub>2</sub>/CH<sub>4</sub> selective adsorption based separations using proprietary synthetic titanosilicate ETS-4 adsorbents [64].

### 1.1.3. Clinoptilolite for CO<sub>2</sub> and N<sub>2</sub> removal from CH<sub>4</sub>

Fig. 1 depicts the framework of clinoptilolite consisting of a two dimensional channel structure [65,66]. Representative chemical formula for the unit cell of clinoptilolite may be simplified to the following expression: (X)<sub>6</sub>(Al<sub>6</sub>Si<sub>30</sub>O<sub>72</sub>)·20H<sub>2</sub>O, where X denotes the exchangeable extra framework cations [68]. Clinoptilolite is a zeolite which has high cation exchange capability [67,69,70]. The distribution of these cations are dependent on their properties (eg: size, charge, etc ...) and coordination with the framework lattice and/or extra framework water molecules [71–76].

Given the small channel aperture of the clinoptilolite micropores, the distribution and type of cations significantly alter the adsorptive performance of this material. Several studies have been conducted to explore the effect of different cation exchanged clinoptilolite types on the potential gas separations including CH<sub>4</sub> upgrading [57,78–84].

While 13X zeolite has been given much of the attention for CO<sub>2</sub>/CH<sub>4</sub> separations (as described in Section 1.1.1), Arefi Pour et al. directly compared natural clinoptilolite and 13X zeolite for this separation [84]. 13X zeolite showed slightly better selectivity than natural clinoptilolite; however systematic cation exchange may improve its CO<sub>2</sub>/CH<sub>4</sub> separation performance. The work of Yang and coauthors is amongst the most detailed and thoroughly investigated in this regard for natural clinoptilolite and its cation exchanged derivatives [57,68,69,85,86]. Results from these studies showed that different cation exchange combinations may result in favourable N<sub>2</sub>/CH<sub>4</sub> selective properties with comparable separation performance to that of titanosilicate ETS-4 [85,86]. This is due to the reduction of the effective channel aperture by the cations, thereby blocking or partially blocking access of CH<sub>4</sub> to the channels. In the case of CH<sub>4</sub> selective adsorption, clinoptilolite cation-exchanged with H<sup>+</sup>, Fe<sup>3+</sup>, Cs<sup>+</sup>, K<sup>+</sup> have shown improved CH<sub>4</sub>/N<sub>2</sub> selectivity [68,81,87]. However, a notable key issue have been the reported slow diffusion kinetics with some of these materials as a result of the small micropore size [57,68,80,88–90]. Frankawitz and Donnelly pointed out that this tends to reduce the performance efficiency of the material in a dynamic PSA environment, especially for CH<sub>4</sub>/N<sub>2</sub> separations. Acid treated clinoptilolite successfully opens the micropores leading to greater CH<sub>4</sub> adsorption, and faster uptake kinetics [68,87]. Similar effects have also been observed particularly for Fe<sup>3+</sup> exchanged clinoptilolite that showed improved adsorption kinetics for CH<sub>4</sub> over natural and Ca<sup>2+</sup> exchanged clinoptilolite [81].

Several modified forms of clinoptilolite show potential for improved separations involving CO<sub>2</sub>, CH<sub>4</sub>, and N<sub>2</sub> gas mixtures. However, only a limited number of studies have investigated the effects of temperature on the adsorption properties and all of these studies have been limited to natural clinoptilolite [82,90,91]. Results from our previous work showed improved separation potential using Ca<sup>2+</sup>, Cs<sup>+</sup>, and Fe<sup>3+</sup> clinoptilolite for these gases [81]. Given the large temperature and pressure distributions present in current natural gas processing facilities, it is prudent to establish the effectiveness of these materials over a broad range of operating conditions. Therefore, in this study, these cation exchanged clinoptilolite types were screened and compared to the natural clinoptilolite for the adsorption separation of CO<sub>2</sub>, CH<sub>4</sub>, and N<sub>2</sub> gases at different temperatures and relatively high pressures.

## 2. Materials and characterization

Natural clinoptilolite was purchased from Ash Meadows Zeolite LLC (Amargosa, NV, USA). The clinoptilolite was received in the powdered form (+140 US. Std. mesh) or as small granules and was sourced from natural deposits located in Amargosa Valley, Nevada in USA. All gases that were used for the experimental analysis were purchased from Linde Canada Ltd. (Ottawa, Ontario, Canada) and had the following specifications for purity: 99.999% for He, 99.999% for N<sub>2</sub>, 99.99% for CH<sub>4</sub>, and 99.99% for CO<sub>2</sub>. The following reagents were used to carry out the cation exchange process: calcium chloride (CaCl<sub>2</sub>, 96.0%, EMD Chemicals Inc., Gibbstown, NJ, USA), cesium chloride (CsCl, 99.0%, Sigma-Aldrich Canada Co., Oakville, Ontario, Canada), and iron (III) chloride hexahydrate (FeCl<sub>3</sub>·6H<sub>2</sub>O, 99.0%, BDH Inc., Toronto, Ontario, Canada). The granular clinoptilolite was crushed to a 60 × 80 US. Std. mesh size prior to commencing the experiments. The adsorbent was washed with deionized water and underwent a cation exchange procedure in the same manner as described in our previous study [81].

In our previous contribution, we verified the phase structure and elemental composition of the clinoptilolite samples using powdered x-ray diffraction (XRD) analysis and electron dispersive spectroscopy (EDS) respectively [81]. The predominant cations present in the original clinoptilolite sample are Ca<sup>2+</sup>, Mg<sup>2+</sup>, and K<sup>+</sup>. Cation exchange

was confirmed for all three clinoptilolite variants (Ca<sup>2+</sup>, Cs<sup>+</sup>, and Fe<sup>3+</sup>). Standard N<sub>2</sub> sorption experiments were performed at 77 K using a Micromeritics ASAP – 2010 volumetric adsorption analyser (Micromeritics, Norcross, GA, USA). The samples were degassed under high vacuum for 8 h at 473 K prior to the experimental analysis. The specific surface area was then calculated from the N<sub>2</sub> sorption data at 77 K, using the Brunauer – Emmett – Teller (BET) method [92]. The micropore volumes were calculated using the Horvath – Kawazoe (HK) approach [93,94].

## 3. Methods and analysis

The equilibrium and kinetic adsorption properties for the clinoptilolite samples were measured using a microgravimetric analyser (VTI Corp., Hialeah, Florida, USA). Details pertaining to the analysis method used are discussed in the [Supplemental Information](#). To properly model the experimental adsorption isotherms across different temperatures, an accurate representation of the adsorption characteristics is required. In this study, the equilibrium adsorption data was regressed using the Sips, Toth, and Dual-Site Langmuir isotherm models which are shown in Equations (1) through (3), respectively. These isotherms are more flexible than the Langmuir approach and account for greater heterogeneity and non-uniformity with respect to adsorbent surfaces compared to the simpler Langmuir isotherm [95–98].

$$\theta = \frac{q}{q_m} = \frac{BP^{1/n}}{1 + (BP)^{1/n}} \quad (1)$$

$$\theta = \frac{q}{q_m} = \frac{BP}{[1 + (BP)^n]^{\frac{1}{n}}} \quad (2)$$

$$q_i = \frac{q_{mA} B_{iA} P}{1 + B_{iA} P} + \frac{q_{mB} B_{iB} P}{1 + B_{iB} P} \quad (3)$$

Here, θ is the fractional coverage; q<sub>m</sub> is the saturation adsorption capacity; B is the Langmuir affinity constant [99]. For the Dual-Site Langmuir Isotherm model, the subscripts A and B represent adsorption sites A and B which are independent of each other. For this model, these two sites reflect the energetic heterogeneity of the adsorbent surface. These sites may correspond with areas close to the exchangeable extra framework cations within the micropores or adsorptive sites elsewhere on the framework [100]. For the Sips and Toth isotherms, the n parameter is dimensionless. When the n parameter is equal to 1, both Equations (1) and (2) reduce to the Langmuir isotherm. However, when the n parameter deviates from 1, this represents increasing heterogeneity of the adsorbent surface. Importantly, the behaviour of the Sips isotherm as pressure approaches the Henry's region is not thermodynamically consistent with the Henry's lower limit for adsorption. This effect is not exhibited by the Toth model which displays the appropriate limits as pressure approaches 0 [101]. None the less, the Sips isotherm may still be a useful tool for practical design purposes.

Adsorption is an exothermic process, therefore the effect of temperature must be considered since adsorption processes are non-isothermal and any change in the column temperature will affect the adsorption capacity. The q<sub>m</sub>, B, and n parameters as functions of temperature for the temperature dependent Sips and Toth isotherm models (given in Equations (1) and (2)) are shown in Equations (4) through (6) [99].

$$B = B_0 e^{\left[ \frac{Q}{RT_0} \right] \left[ \frac{T_0}{T} - 1 \right]} \quad (4)$$

$$q_m = q_{m0} e^{\chi \left[ 1 - \frac{T}{T_0} \right]} \quad (5)$$

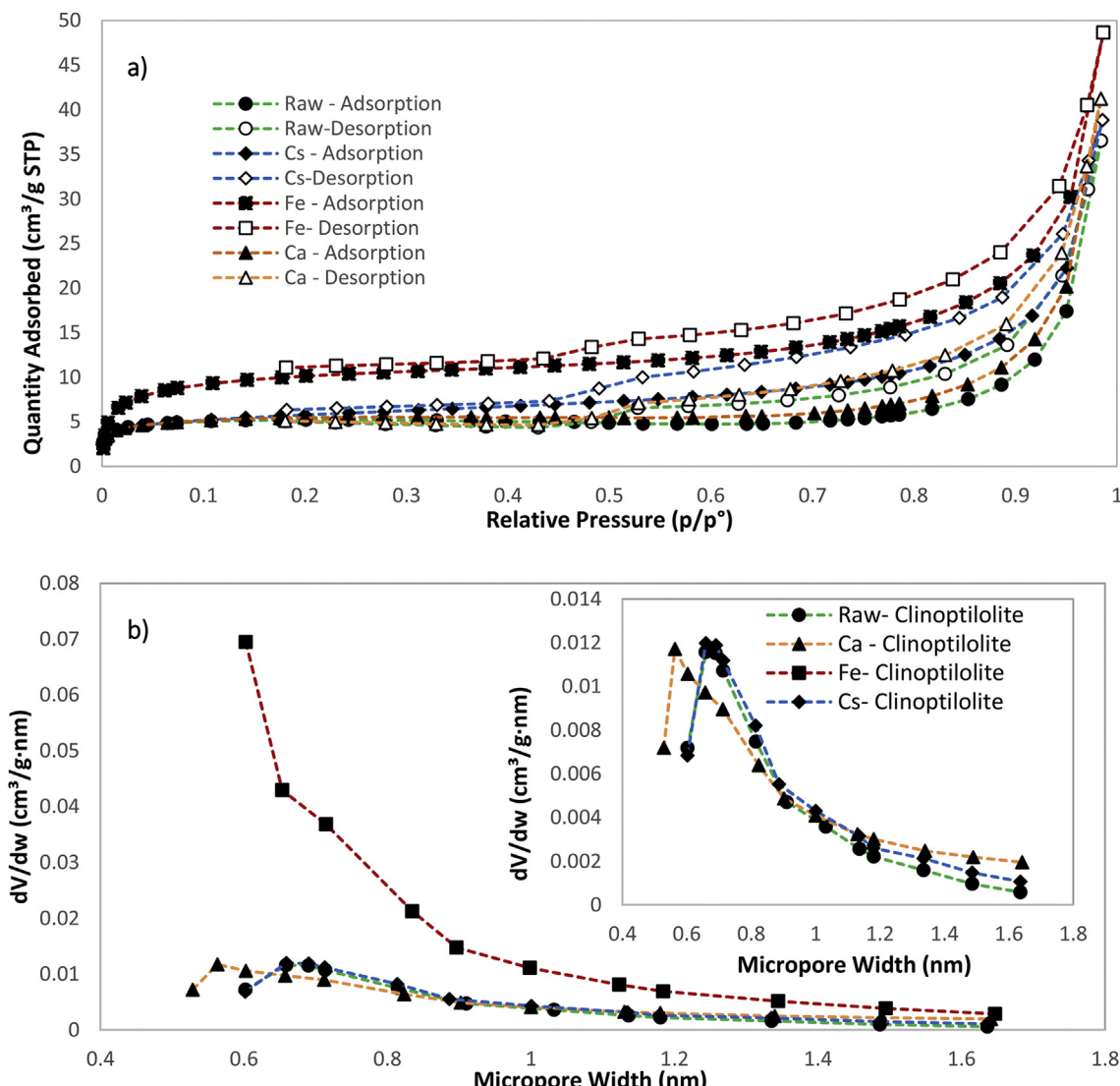


**Fig. 2.** a) N<sub>2</sub> adsorption (solid symbols) –desorption (open symbols) isotherms for raw, Ca<sup>2+</sup>, Cs<sup>+</sup>, and Fe<sup>3+</sup> cation exchanged clinoptilolite at 77 K. b) Distribution of the micropores for raw, Ca<sup>2+</sup>, Cs<sup>+</sup>, and Fe<sup>3+</sup> cation exchanged clinoptilolite determined from the sorption experiments with N<sub>2</sub> at 77 K using the HK distribution method.

$$n = n_0 + \alpha_n \left[ 1 - \frac{T}{T_0} \right] \quad (6)$$

Here,  $B_0$  is the adsorption affinity constant at reference temperature  $T_0$ ,  $q_{m0}$  is the saturation adsorption capacity at  $T_0$ , and  $n_0$  is the parameter  $n$  at  $T_0$ , whereas  $\chi$  and  $\alpha_n$  are constant parameters. Substitution of Equations (4) through (6) into Equations (1) and (2) will give six parameter functions where the parameters ( $B_0$ ,  $Q$ ,  $q_{m0}$ ,  $\chi$ ,  $n_0$ ,  $\alpha_n$ ) are obtained by regressing the model to fit the experimental data obtained at different temperatures.

Similarly, the temperature dependent parameters for the Dual-Site Langmuir model given in Equation (3) are described in Equations (7) and (8) [102].

$$q_m = k_1 - k_2 T \quad (7)$$

$$B = k_3 e^{\left[ \frac{k_4}{T} \right]} \quad (8)$$

The  $k_1$ ,  $k_2$ ,  $k_3$ , and  $k_4$  constants are thus determined by fitting experimental data obtained at different temperatures. The model that best described the experimental data was determined by the lowest sum of the squared residuals (SSR).

The concentration pulse chromatography technique was used to determine the CO<sub>2</sub>, CH<sub>4</sub>, and N<sub>2</sub> Henry's Law adsorption constants ( $K_p$ ) [103–106]. Details pertaining to the analysis method used are discussed in the *Supplemental Information*.

The dimensional  $K_p$  values are measured at different temperatures. The limiting heat of adsorption ( $\Delta H$ ) is thus calculated from the slope of the van't Hoff plot ( $\ln K_p$  vs.  $1/T$ ) as shown in Equation (9), where  $K_0$  is the pre-exponential constant for Henry's law constant,  $K$ , and  $R$  is the gas constant.

$$K = K_0 e^{\left[ \frac{-\Delta H}{RT} \right]} \quad (9)$$

The adsorbate-adsorbent interactions at different temperatures

**Table 1**

BET surface area, HK micropore volume, and total pore volume for raw,  $\text{Ca}^{2+}$ ,  $\text{Cs}^+$ , and  $\text{Fe}^{3+}$  cation exchanged clinoptilolite determined from the sorption experiments with  $\text{N}_2$  at 77 K.

Sample	BET Surface area ( $\text{m}^2/\text{g}$ )	HK Micropore volume ( $\text{cm}^3/\text{g}$ )	Micropore area ( $\text{m}^2/\text{g}$ )	Total pore volume ( $\text{cm}^3/\text{g}$ )	Average pore diameter ( $\text{\AA}$ )
raw clinoptilolite	19.0861	0.007068	15.7022	0.054171	292.213
Cs – clinoptilolite	18.8545	0.006262	13.9378	0.060032	288.338
Fe – clinoptilolite	121.1814	0.046986	18.1502	0.068392	168.991
Ca - clinoptilolite	20.4073	0.003460	12.6242	0.061328	188.150

manifest itself in the isosteric heat of adsorption which is a good indicator of the adsorption strength [107]. The isosteric heat of adsorption,  $\Delta H$ , is calculated at zero fractional loading as shown in Equation (9). Under the Langmuir assumption  $\Delta H$  is constant, as it is considered to be independent of surface coverage. In reality, the isosteric heat of adsorption may be slightly variable, as it is effected by the local surface heterogeneity and additional molecular interactions which occur at higher loadings. This effect may be observed by calculating the  $\Delta H$  directly from experimental isotherms at different temperatures using the Clausius-Clapeyron equation.

$$\left( \frac{\Delta H_{iso}}{R} \right) = \left( \frac{\partial \ln P}{\partial \left( \frac{1}{T} \right)} \right)_q \quad (10)$$

According to this equation, the change in natural logarithm of pressure (P) with respect to the change in inverse temperature (T) at constant q is related to heat of adsorption.  $\Delta H$  is determined from the slope of the plot of  $\ln(P)$  against  $1/T$  at constant q.

Adsorption kinetics is an important factor to consider when evaluating adsorbent performance, as well. In our previous paper, we showed that the Linear Driving Force (LDF) model can be an acceptable tool to rapidly quantify the kinetic uptake data for comparison purposes between different materials [81]. The LDF model is shown in Equation (11a) [91,95,107–112].

$$\frac{\partial q}{\partial t} = k_{LDF}(q_e - q(t)) \quad (11a)$$

$$k_{LDF} \approx \frac{15D_e}{R_p^2} \quad (11b)$$

The dynamic system response to a pressure step change is measured as the change in q as a function of time, t. The uptake rate,  $dq/dt$ , is plotted as a function of ( $q_e - q(t)$ ) at different times, and the slope of this plot gives the mass transfer coefficient,  $k_{LDF}$ , that is specific to the system. As shown in Equation (11b),  $k_{LDF}$  can be interpreted as diffusion time constant,  $D_e/R_p^2$ , to better reflect intracrystalline diffusion within the zeolite [107]. However, as reported by others, this method is only valid strictly for comparison purposes and has no practical application in overall PSA design due to existing limitations inherent with respect to the measuring approach [54,109].

Regarding a particular gas mixture separation the ideal selectivity,  $\alpha_{1/2}$ , is calculated as the ratio of the pure component adsorption capacities ( $q_1$  and  $q_2$ ) at the same temperature and pressure for gases 1 and 2 [28,54]. However, this approach is limited as it assumes that there is

no interaction between the different gases that are adsorbed.

$$\alpha_{1/2} = \frac{q_1}{q_2} \quad (12)$$

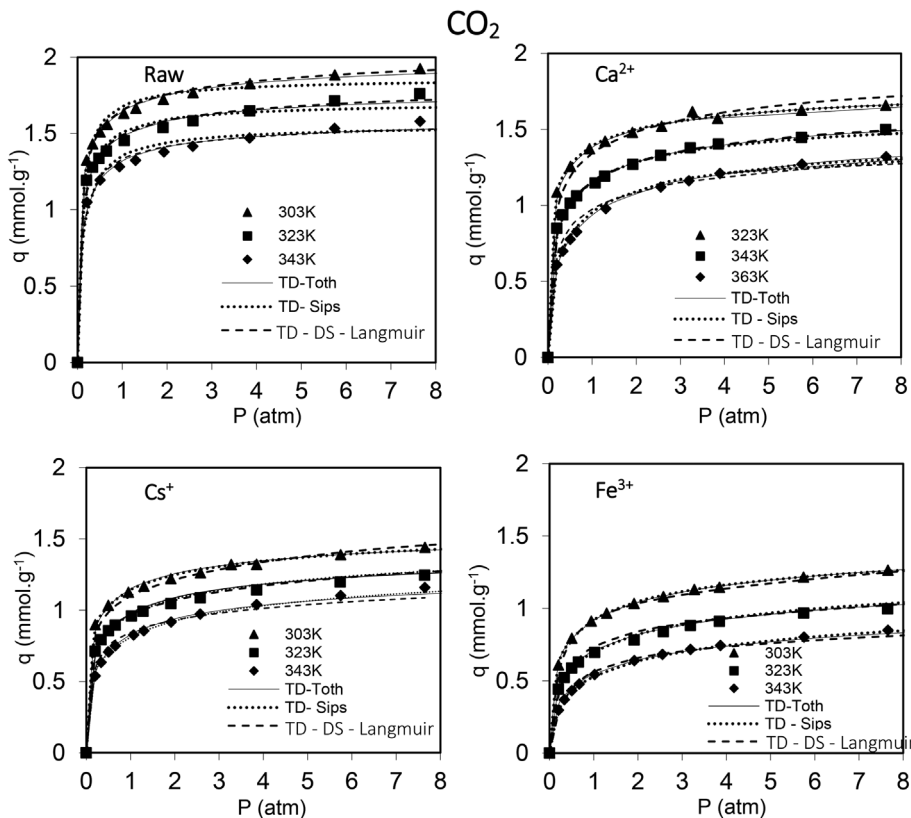
#### 4. Results and discussion

Fig. 2A presents the experimental adsorption-desorption isotherms as a function of relative pressure for  $\text{N}_2$  at 77 K on the raw and cation exchanged clinoptilolite samples. The  $\text{N}_2$  adsorption – desorption behaviour is similar for all of the clinoptilolite types and shares the similar characteristics as others have reported in the literature [70,90]. It may be summarized as follows: At low relative pressures ( $P/P_o$  below 0.1) an initial increase in  $\text{N}_2$  adsorption is observed. Between the values of  $0.1 < P/P_o < 0.8$  the  $\text{N}_2$  adsorption isotherms stay relatively consistent and only begin to increase quickly again at relative pressures greater than 0.8. Desorption behaviour shows the presence of a hysteresis loop at relative pressures in the range of  $0.5 < P/P_o < 1$  for all of the clinoptilolite types. The increase in  $\text{N}_2$  adsorption at low relative pressure is expected for these materials and shows presence of microporosity. Whereas, the shape of the adsorption curve above relative pressures of 0.8 indicates the presence of mesopores and macropores. The hysteresis loop, is characteristic of clinoptilolites samples, and can be attributed to factors such as multilayer adsorption and capillary condensation within the mesopore space [54].

The micropore size of clinoptilolite is only slightly larger than the size of  $\text{N}_2$ . Therefore, at the experimental temperatures of 77 K,  $\text{N}_2$  diffusion within the pores of clinoptilolite is difficult, which may result in a reduction in the measured adsorption  $\text{N}_2$ . This means that the estimated surface area calculated using the BET model may not account for all of the micropore space. While the HK and BET methods may not accurately depict the adsorbent surface characteristics, they can still present valuable information, and have thus been used by many contributions in the literature. A summary of the calculated pore properties and surface area of the adsorbents is provided in Table 1. As can be seen from this table, the calculated BET surface area is the highest for  $\text{Fe}^{3+}$  variant compared to the other forms of clinoptilolite. This trend is indicative of the limited access of  $\text{N}_2$  to the micropores as previously discussed. Fig. 2b shows the distribution of the micropore volume for raw,  $\text{Ca}^{2+}$ ,  $\text{Cs}^+$ , and  $\text{Fe}^{3+}$  cation exchanged clinoptilolite determined from the  $\text{N}_2$  sorption experiments using the Horvath-Kawazoe (HK) method. The calculated effective micropore volume for the different types of clinoptilolite is in the order of:  $\text{Fe}^{3+} > \text{raw} \approx \text{Cs}^+ > \text{Ca}^{2+}$ . From Fig. 2b, it is clear that the  $\text{Fe}^{3+}$  cation exchanged clinoptilolite likely has a more open micropore structure compared to the other three types of clinoptilolite studied, thus allowing access to  $\text{N}_2$ .

##### 4.1. Pure component $\text{CO}_2$ , $\text{CH}_4$ and $\text{N}_2$ adsorption equilibria

The pure  $\text{CO}_2$ ,  $\text{CH}_4$ , and  $\text{N}_2$  adsorption isotherms were determined for raw,  $\text{Ca}^{2+}$ ,  $\text{Cs}^+$ , and  $\text{Fe}^{3+}$  cation exchanged clinoptilolite at different temperatures for pressures up to 8 atm. Figs. 3 through 5 show these experimental adsorption isotherms and the temperature dependent (TD) Toth, Sips, and Dual-Site (DS) Langmuir model fits for each adsorbent. Table 2 presents the calculated parameters for these adsorption isotherm models. The accuracy of these models is assessed using the SSR values between the calculated and experimental results. All of the experimental adsorption isotherms conform to the expected behaviour: adsorption capacity is shown to increase with increasing pressure and decreasing temperature.



**Fig. 3.** Experimentally determined adsorption isotherms for  $\text{CO}_2$  at different temperatures for raw clinoptilolite compared to  $\text{Fe}^{3+}$ ,  $\text{Ca}^{2+}$ , and  $\text{Cs}^+$  exchanged samples. The experimental data points were fitted with temperature dependant Toth, Sips, and Dual Site Langmuir models.

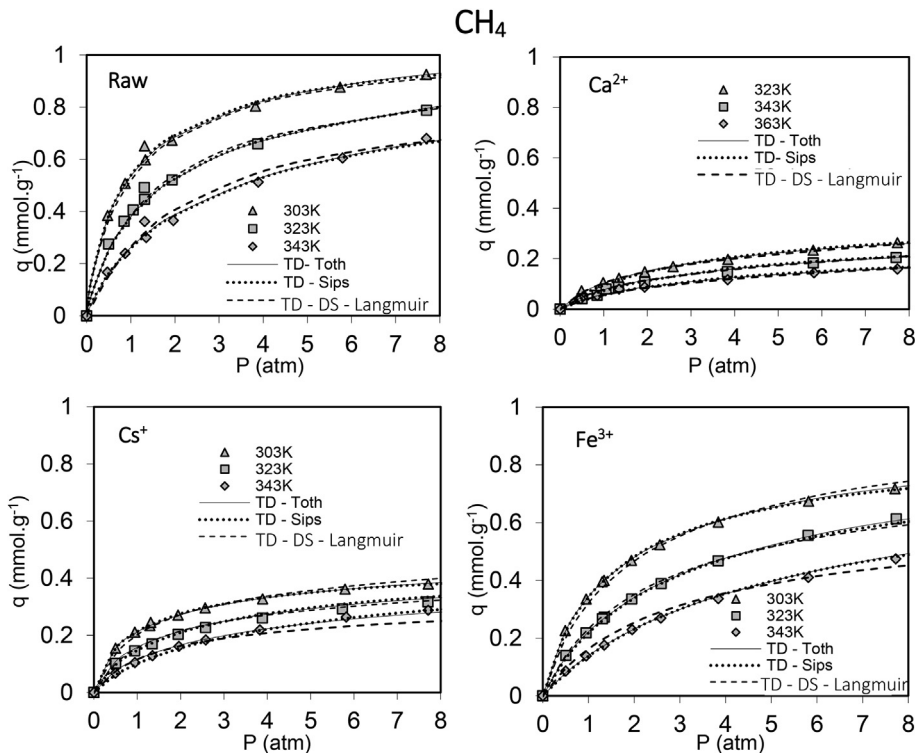


**Fig. 4.** Experimentally determined adsorption isotherms for  $\text{CH}_4$  at different temperatures for raw clinoptilolite compared to  $\text{Fe}^{3+}$ ,  $\text{Ca}^{2+}$ , and  $\text{Cs}^+$  exchanged samples. The experimental data points were fitted with temperature dependant Toth, Sips, and Dual Site Langmuir models.

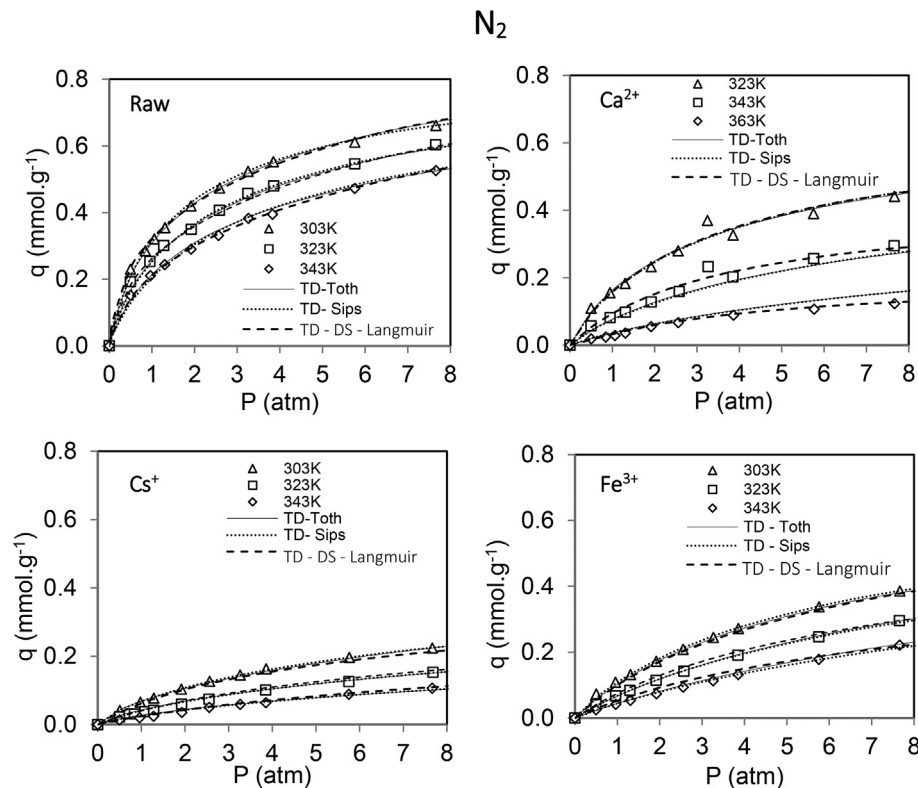


**Fig. 5.** Experimentally determined adsorption isotherms for  $\text{N}_2$  at different temperatures for raw clinoptilolite compared to  $\text{Fe}^{3+}$ ,  $\text{Ca}^{2+}$ , and  $\text{Cs}^+$  exchanged samples. The experimental data points were fitted with temperature dependant Toth, Sips, and Dual Site Langmuir models.

**Table 2**

Temperature dependent Sips, Toth, and Dual Site Langmuir model parameters for  $\text{CO}_2$ ,  $\text{CH}_4$  and  $\text{N}_2$  adsorption on raw clinoptilolite and  $\text{Ca}^{2+}$ ,  $\text{Cs}^+$ , and  $\text{Fe}^{3+}$  cation-exchanged clinoptilolites. The shaded area denotes the lowest values for the Summed Squared Residuals (SSR) between the experimental values and the temperature dependent isotherm models.

Model	Parameter	Clinoptilolite Type											
		Raw			$\text{Ca}^{2+}$			$\text{Cs}^+$			$\text{Fe}^{3+}$		
		$\text{CO}_2$	$\text{CH}_4$	$\text{N}_2$	$\text{CO}_2$	$\text{CH}_4$	$\text{N}_2$	$\text{CO}_2$	$\text{CH}_4$	$\text{N}_2$	$\text{CO}_2$	$\text{CH}_4$	$\text{N}_2$
TD – Toth	$n_0$ (mmol/g)	0.493	0.692	0.574	0.434	0.617	0.740	0.405	0.538	0.316	0.315	0.757	0.870
	$\alpha_n$	0.851	0.025	0.001	0.000	0.003	0.002	0.045	0.194	0.175	0.002	0.200	0.002
	$X$	1.759	0.493	0.948	0.811	2.986	3.659	1.279	0.598	4.605	2.179	0.019	0.066
	$T_0$ (K)	303.15	303.15	303.15	323.15	323.15	323.15	303.15	303.15	303.15	303.15	303.15	303.15
	$Q$ (kJ/mol)	20.995	26.951	9.440	39.150	7.293	33.321	21.374	25.362	13.160	21.820	29.769	20.785
	$q_{mo}$ (mmol/g)	2.061	1.168	1.122	1.911	0.462	0.743	1.697	0.564	2.133	1.883	0.978	0.736
	$b_0$ (atm <sup>-1</sup> )	77.376	1.616	0.848	77.376	0.505	0.374	77.391	1.969	0.116	77.389	0.778	0.175
SSR		0.031	0.003	0.003	0.008	0.001	0.013	0.012	0.001	0.002	0.004	0.001	0.001
TD – Sips	$n_0$ (mmol/g)	1.155	1.175	1.207	2.088	1.100	1.136	2.494	1.301	1.248	2.059	1.090	1.075
	$\alpha_n$	0.007	0.003	0.000	1.188	0.000	0.000	0.001	0.755	0.001	0.001	0.389	0.006
	$X$	1.347	0.669	0.451	1.674	3.343	3.429	0.636	0.057	2.620	1.668	0.658	0.464
	$T_0$ (K)	303.15	303.15	303.15	323.15	323.15	323.15	303.15	303.15	303.15	303.15	303.15	303.15
	$Q$ (kJ/mol)	6.916	22.190	11.451	12.921	3.653	29.695	13.067	23.689	15.041	14.127	24.329	20.228
	$q_{mo}$ (mmol/g)	1.867	1.084	0.882	1.879	0.388	0.717	1.766	0.477	0.515	1.612	0.890	0.710
	$b_0$ (atm <sup>-1</sup> )	8.782	0.984	0.555	2.833	0.325	0.283	1.832	0.803	0.152	1.325	0.623	0.180
SSR		0.084	0.004	0.005	0.014	0.002	0.014	0.013	0.002	0.002	0.003	0.002	0.001
TD - DS Langmuir	$K_{11}$ (mmol/g)	1.465	1.199	0.815	1.838	0.871	3.778	2.470	1.343	1.070	3.639	2.030	1.643
	$K_{21}$ (mmol/g K)	0.004	0.001	0.000	0.004	0.002	0.010	0.005	0.003	0.001	0.009	0.005	0.004
	$K_{31}$ (atm <sup>-1</sup> )	0.103	0.009	0.008	0.153	0.056	0.147	0.415	0.102	0.006	0.005	0.009	0.036
	$K_{41}$ (K)	274.6	1337.2	906.8	274.6	854.4	200.4	1053.2	704.2	100.6	610.0	1330.0	85.17
	$K_{12}$ (mmol/g)	3.847	1.227	0.862	3.917	395.51	0.515	2.755	2.640	1.217	3.578	1.594	1.593
	$K_{22}$ (mmol/g K)	0.0071	0.0036	0.0018	0.0082	0.0047	0.0015	0.0069	0.0067	0.0032	0.0083	0.0040	0.0040
	$K_{32}$ (atm <sup>-1</sup> )	1.5085	0.6486	0.0232	1.5380	0.0000	0.6339	0.0574	0.0099	0.0113	0.0482	0.0384	0.0516
	$K_{42}$ (K)	660.4	843.3	1503.6	660.4	894.0	354.0	373.8	109.0	1003.0	1406.1	433.3	493.42
SSR		0.044	0.009	0.001	0.073	0.001	0.007	0.035	0.005	0.001	0.020	0.009	0.003

**Table 3**  
CO<sub>2</sub>, CH<sub>4</sub>, and N<sub>2</sub> gas properties [115].

Gas	Kinetic diameter (Å)	Polarizability ( $\times 10^{-25}$ cm <sup>3</sup> )	Quadrupole moment (x $10^{-26}$ esu·cm <sup>2</sup> )
CO <sub>2</sub>	3.33	26.5	4.30
CH <sub>4</sub>	3.80	26.0	0
N <sub>2</sub>	3.64	17.6	1.52

**Table 4**  
Physical properties of the zeolite extra framework cations [116,117].

Cation	Effective Ionic Radius (Å)	Hydrated Radius (Å)	Charge to Ionic Radius Ratio
Fe <sup>3+</sup>	0.55	1.40	5.45
Mg <sup>2+</sup>	0.72	1.50	2.78
Ca <sup>2+</sup>	1.00	1.80	2.00
Na <sup>+</sup>	1.02	1.80	0.98
K <sup>+</sup>	1.38	2.20	0.72
Cs <sup>+</sup>	1.67	2.60	0.59

Looking down each column in Table 2, the SSR values for each model fit are directly compared for each individual isotherm. Among the three isotherm models used in this study, in most cases the experimental adsorption data is better represented by the TD-Toth model as shown in Table 2 where the lowest SSR values are highlighted for each isotherm. In principle, the extra parameters used with Dual-Site Langmuir model should give this isotherm model greater flexibility compared to the other isotherm types. However, the temperature dependent parameters for the Dual-Site Langmuir model that have been proposed in the literature and thus used in this study are inherently more restrictive compared to those of the TD Toth and Sips equations. This temperature variance is represented as a linear function for the DS Langmuir model and is limited only to changes in the adsorption affinity parameter and saturation adsorption capacity with temperature. This is compared to the temperature variation being modelled as an Arrhenius type relationship for the Sip and Toth isotherms. Additionally, this behaviour is extended to not only the *B* and *q* parameters, but also the dimensionless surface parameter, *n*, for the Sips and Toth isotherms. It is supposed that the DS Langmuir model may be modified in a similar context, particularly as it relates to the *q* parameter. However, this will result in an isotherm equation which is far more complicated than that depicted in Equations (3), (7) and (8) and is beyond the scope of this current study. In its current form, the temperature dependence in the *q<sub>m</sub>* parameter is modelled as a linear function. This function inherently implies that at some temperature the saturation adsorption capacity will be negative, which is not possible. Since the temperature dependence can only be modelled accurately over a limited temperature range, careful attention must be given to ensure that the results are thermodynamically consistent.

As can be seen in Figs. 3 through 5, the adsorption behaviour of the different gases on the clinoptilolite samples is different, which is typical for this material [57,58,68,86,90,113]. In general, CO<sub>2</sub> is the most adsorbed gas on the clinoptilolite, followed by CH<sub>4</sub> and then N<sub>2</sub>, (the exception being Ca<sup>2+</sup> clinoptilolite where more N<sub>2</sub> is adsorbed compared to CH<sub>4</sub>). This behaviour is influenced by both the characteristics of the modified zeolite and the properties of the adsorbate; both of which ultimately govern the effect of the adsorption interaction parameters [95,114]. Tables 3 and 4 show the relevant properties of the adsorbed gases and the zeolite extra framework cations which are important to better understand their implication on the experimental observations.

As shown in Table 3, CO<sub>2</sub> has a larger polarizability and quadrupole moment compared to CH<sub>4</sub> and N<sub>2</sub> which result in greater electrostatic potential for CO<sub>2</sub>. Therefore, the higher capacity for CO<sub>2</sub> gas can be explained by the quadrupole interaction with the cations present on the

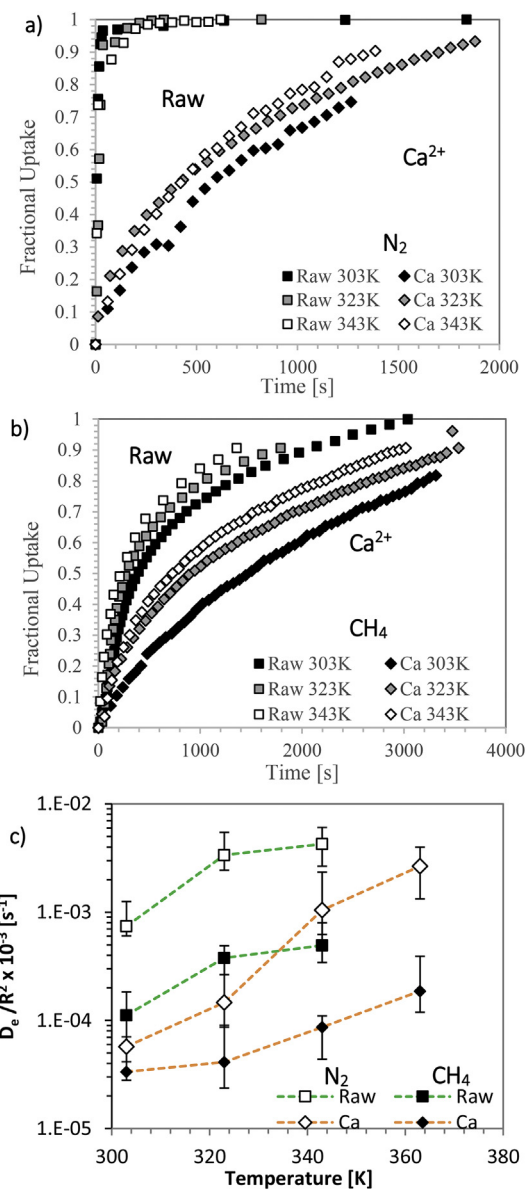


**Fig. 6.** a) Experimental adsorption fractional uptake rate curves for a) N<sub>2</sub> and b) CH<sub>4</sub> gas adsorption on raw and Ca<sup>2+</sup> clinoptilolite samples determined at 303 K, 323 K, and 343 K with a pressure step change from 0.5 to 1 atm. c) Experimentally determined diffusion time constants calculated from the LDF model as a function of temperature for N<sub>2</sub> and CH<sub>4</sub> gas adsorption on raw and Ca<sup>2+</sup> clinoptilolite samples. For graph c) the solid points are CH<sub>4</sub> and the hollow points are N<sub>2</sub>, the dash lines are to guide the eye.

zeolite surface. However, the trend in CO<sub>2</sub> adsorption is nuanced, whereby the sequence of adsorption on the clinoptilolite is in the following order: Fe<sup>3+</sup> < Cs<sup>+</sup> < Ca<sup>2+</sup> < Raw. Some factors that influence CO<sub>2</sub> adsorption behaviour include the cation type and the distribution in relation to the zeolite framework. These cations impact the surface electrostatic potential and local acid/base environment [118–120]. The raw clinoptilolite exhibits the greatest amount of CO<sub>2</sub> adsorption. The composition and distribution of cations within the raw clinoptilolite consist of a mix of alkali and alkali earth cations (predominately Mg<sup>2+</sup>, Ca<sup>2+</sup>, and K<sup>+</sup>) whereby none of the cations are dominant. The cationic variability induces increased surface charge heterogeneity which is conducive to stronger electrostatic interactions. This is supported by the fact that the raw clinoptilolite also shows the highest adsorption capacity for both CH<sub>4</sub> and N<sub>2</sub> in comparison to all of the other cation exchanged variants studied as well. In contrast, Fe<sup>3+</sup>

**Table 5**

Average Henry's Law constants at different temperatures as determined with CPM for CO<sub>2</sub>, CH<sub>4</sub> and N<sub>2</sub> gases on raw clinoptilolite compared to Fe<sup>3+</sup>, Ca<sup>2+</sup>, and Cs<sup>+</sup> exchanged samples.

T(K)	Raw Clino.	Ca <sup>2+</sup> Clino.	Cs <sup>+</sup> Clino.	Fe <sup>3+</sup> Clino.
	K <sub>p</sub> <sup>a</sup> (mmol·g <sup>-1</sup> ·atm <sup>-1</sup> )	K <sub>p</sub> <sup>a</sup> (mmol·g <sup>-1</sup> ·atm <sup>-1</sup> )	K <sub>p</sub> <sup>a</sup> (mmol·g <sup>-1</sup> ·atm <sup>-1</sup> )	K <sub>p</sub> <sup>a</sup> (mmol·g <sup>-1</sup> ·atm <sup>-1</sup> )
<b>CO<sub>2</sub></b>				
428			0.738 ± 0.026	0.656 ± 0.015
443			0.500 ± 0.018	0.539 ± 0.007
458			0.348 ± 0.042	0.414 ± 0.012
473			0.258 ± 0.025	0.313 ± 0.021
488			0.201 ± 0.011	0.261 ± 0.010
503	3.144 ± 0.073	1.868 ± 0.087	0.135 ± 0.038	0.222 ± 0.004
518	2.586 ± 0.063	1.513 ± 0.084		
533	2.068 ± 0.036	1.180 ± 0.041		
548	1.789 ± 0.046	0.802 ± 0.019		
563	1.480 ± 0.039	0.648 ± 0.029		
<b>CH<sub>4</sub><sup>b</sup></b>				
303	0.334 ± 0.042	0.083 ± 0.028	0.216 ± 0.009	0.851 ± 0.017
318	0.324 ± 0.013	0.060 ± 0.060	0.206 ± 0.016	0.700 ± 0.018
333	0.301 ± 0.026	0.067 ± 0.067	0.204 ± 0.008	0.631 ± 0.006
348	0.273 ± 0.054	0.057 ± 0.057	0.188 ± 0.017	0.507 ± 0.019
363	0.227 ± 0.086	0.052 ± 0.052	0.181 ± 0.019	0.399 ± 0.006
<b>N<sub>2</sub><sup>b</sup></b>				
303	0.401 ± 0.028	0.129 ± 0.012	0.194 ± 0.008	0.460 ± 0.007
318	0.351 ± 0.107	0.114 ± 0.022	0.195 ± 0.007	0.387 ± 0.005
333	0.323 ± 0.069	0.089 ± 0.014	0.189 ± 0.002	0.324 ± 0.042
348	0.201 ± 0.063	0.071 ± 0.022	0.186 ± 0.004	0.290 ± 0.006
363	0.168 ± 0.075	0.056 ± 0.004	0.180 ± 0.006	0.227 ± 0.018

<sup>a</sup> K<sub>p</sub> = average of n = 3 individual experiments with the range as the standard deviation. The experimental uncertainty u (K<sub>p</sub>) ≈ 13.5%.

<sup>b</sup> The calculated CH<sub>4</sub> and N<sub>2</sub> experimental K<sub>p</sub> values determined from the CPM method are too low to be considered reliable.

clinoptilolite has the lowest CO<sub>2</sub> capacity, despite being the smallest cation with the greatest charge density among the studied cations. This behaviour runs counter to previous reports which show that in general, smaller extra framework cations (H<sup>+</sup>) result in greater CO<sub>2</sub> adsorption on zeolites [119]. CO<sub>2</sub> is a moderate Lewis acid, therefore its adsorption behaviour is dictated by the local acid–base surface properties of the zeolite. Extra framework cations provide acid sites and the framework oxygen atoms nearest to the cation act as basic sites. The charge of a particular site is influenced by the position and type of extra framework cation in relation to the framework oxygen atoms [118–120]. In principle, three negative framework charges are required to be balanced with each individual Fe<sup>3+</sup> cation. However, transition metal cations such as Fe<sup>3+</sup> may react to form additional oxygen containing compounds onto the zeolite surface [121–123]. To the best of our knowledge, this behaviour has not been documented in the case of Cs<sup>+</sup> or Ca<sup>2+</sup> cation exchanged zeolite variants. This means that for the Fe<sup>3+</sup> clinoptilolite, there is likely increased opportunity for basicity of the framework. It has also been hypothesized that the zeolite framework may be partially dealuminated following Fe<sup>3+</sup> cation exchange as evidenced by changes in the Si/Al ratio and decreased crystallinity observed through XRD [81]. It is likely that the combination of these effects results in the total amount adsorbed being the lowest for CO<sub>2</sub> on the Fe<sup>3+</sup> clinoptilolite.

It is evident that the overall adsorption capacity of CO<sub>2</sub> on the Cs<sup>+</sup> clinoptilolite is lower than the raw clinoptilolite. The Cs<sup>+</sup> cation is the largest and has the lowest charge density of the studied cations exchanged into the clinoptilolite. These combined effects, in addition to the large molecular weight of Cs<sup>+</sup> may be detrimental to the overall CO<sub>2</sub> uptake [84,119]. Based on this behaviour, it is likely that the Cs<sup>+</sup> cation is occupying the space within the pore cavity but is not actually blocking the channels. While this limits the overall gas uptake, it has

little effect on the microporous diffusion resistance to the same extent as Ca<sup>2+</sup> clinoptilolite as documented in our previous study [81].

The adsorption of CH<sub>4</sub> on the clinoptilolite is in the following order: Ca<sup>2+</sup> < Cs<sup>+</sup> < Fe<sup>3+</sup> < Raw, whereas the adsorption of N<sub>2</sub> is in the order of Cs<sup>+</sup> < Fe<sup>3+</sup> < Ca<sup>2+</sup> < Raw. Both CO<sub>2</sub> (3.33 Å) and N<sub>2</sub> (3.64 Å) are smaller than CH<sub>4</sub> (3.80 Å). With respect to Ca<sup>2+</sup> clinoptilolite, CH<sub>4</sub> adsorption is restricted since it cannot access the pores at all [80,90]. Therefore, for the Ca<sup>2+</sup> clinoptilolite it is likely that the pore aperture is limited due to the positioning of the Ca<sup>2+</sup> cation within the channels. With the exception of the Ca<sup>2+</sup> clinoptilolite, preferential adsorption of CH<sub>4</sub> compared to N<sub>2</sub> is observed for all clinoptilolite types, and follows similar patterns as the CO<sub>2</sub> adsorption mechanism. Since clinoptilolite has a variable surface charge distribution, the higher polarizability of CH<sub>4</sub> means that it has a greater tendency to form instantaneous dipoles with the surface. This effect allows for greater surface occupancy compared to N<sub>2</sub>.

Microporous diffusion resistance is dominant for natural clinoptilolite and many of its derivatives [88,113]. For gas separations involving CH<sub>4</sub> the influence of the dynamic behaviour on the adsorption separation performance for this material is profound. Some studies even report N<sub>2</sub>/CH<sub>4</sub> kinetic selectivity to be in the 100's for Mg<sup>2+</sup>, Ni<sup>2+</sup>, or Li<sup>+</sup> cation exchanged clinoptilolite among many [58,81,113]. In this study, with respect to the Cs<sup>+</sup> and Fe<sup>3+</sup> clinoptilolite, the studied adsorbates are known to diffuse with less resistance within the micropores and have little if any kinetic selectivity [81]. Therefore, the channels are likely not as obstructed by the presence of the extra framework Cs<sup>+</sup> or Fe<sup>3+</sup> cations to the same extent as the raw or Ca<sup>2+</sup> clinoptilolite. Since, CH<sub>4</sub> is the slowest adsorbing of the studied gases [59,81]; this essentially presents the lower limit for diffusional uptake. Slower kinetic behaviour elongates the effective adsorption/desorption propagation fronts and contributes to reduced separation performance in

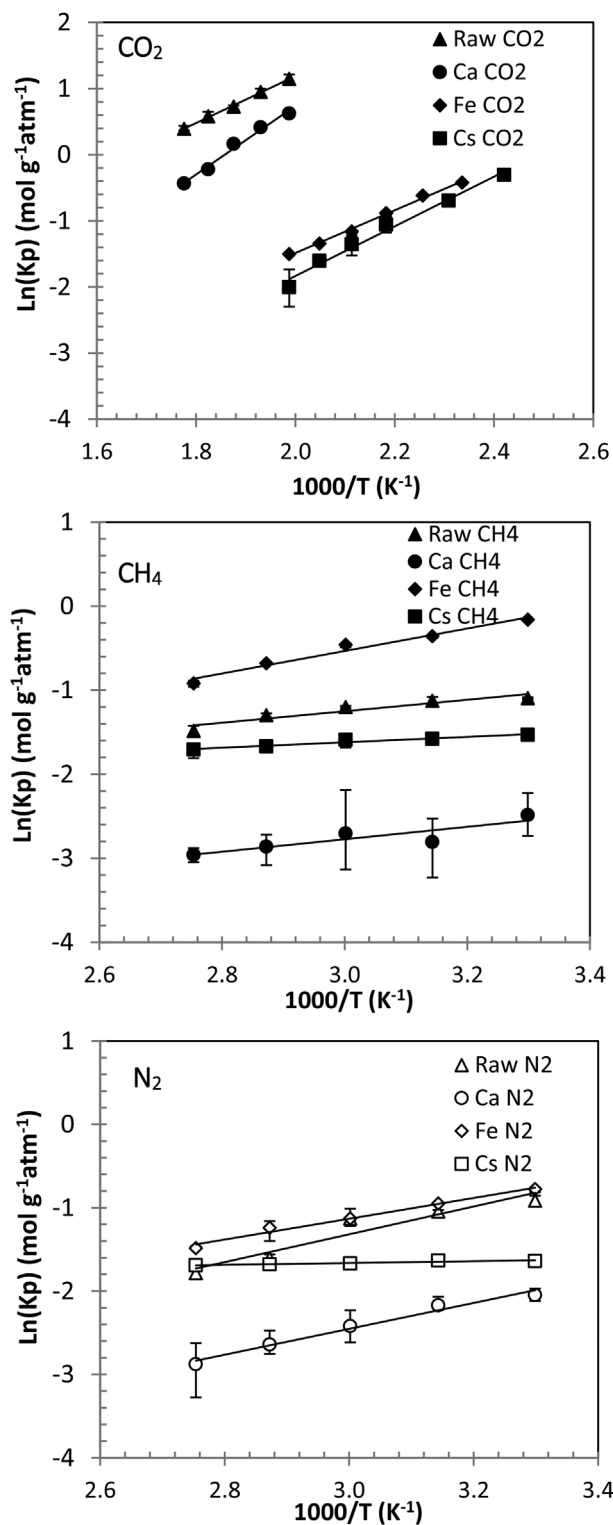


**Fig. 7.** van't Hoff plots of the average Henry's Law constants for pure component  $\text{CO}_2$ ,  $\text{CH}_4$ , and  $\text{N}_2$  injections into helium carrier gas, as a function of inverse temperature using the CPM method. The error bars represent the maximum and minimum experimental  $K_p$  values for the repeats.

dynamic adsorption environments. Fig. 6 depicts the kinetic adsorption uptake rates in response to a pressure step change for  $\text{CH}_4$  and  $\text{N}_2$  on raw and  $\text{Ca}^{2+}$  modified clinoptilolite. The corresponding diffusion constants for  $\text{CH}_4$  are presented and these values are compared to  $\text{N}_2$  at different temperatures for raw and  $\text{Ca}^{2+}$  clinoptilolite. Due to the modest  $\text{CH}_4/\text{N}_2$  adsorption equilibrium selectivity for raw and  $\text{Ca}^{2+}$

**Table 6**

Experimental limiting heat of adsorption values for  $\text{CO}_2$ ,  $\text{CH}_4$  and  $\text{N}_2$  with raw and different cation exchanged clinoptilolite determined using the CPM method.

Adsorbent	Experimental $-\Delta H$ ( $\text{kJ}\cdot\text{mol}^{-1}$ )		
	$\text{CO}_2$	$\text{CH}_4^{\text{a}}$	$\text{N}_2^{\text{a}}$
Raw Clinoptilolite	29.3	5.7	13.9
$\text{Ca}^{2+}$ Clinoptilolite	43.1	6.4	12.9
$\text{Cs}^+$ Clinoptilolite	31.2	1.0	2.8
$\text{Fe}^{3+}$ Clinoptilolite	27.8	9.7	9.6

<sup>a</sup> The calculated  $\text{CH}_4$  and  $\text{N}_2$  experimental  $-\Delta H$  values determined from the CPM method are considered not accurate due to the very low  $K_p$  values obtained.

clinoptilolite, the influence of the molecular dynamics becomes more meaningful for this separation. There is a positive correlation between the microporous diffusion rate and temperature which is to be expected based upon the increased kinetic energy of the molecules. For  $\text{CH}_4$ , some notable diffusional resistance exists for the raw clinoptilolite which is likely due to the mix of cations present in the natural deposits. The diffusion constants for both gases are the lowest for the pore blocking  $\text{Ca}^{2+}$  exchanged clinoptilolite, as can be seen from Fig. 6c. These findings suggest that higher temperature is required in order to achieve more efficient separation. However, this will ultimately need to be balanced with subsequent reduced adsorption capacity and changes to the gas adsorption equilibrium selectivity at different temperatures.

#### 4.2. Henry's law constant and heat of adsorption

In Henry's Law region, adsorbate–adsorbent forces are the most dominant adsorption mechanism since at near zero coverage additional forces which are dependent on adsorbate–adsorbate effects are minimized. The experimental Henry's Law constants were determined for pure  $\text{CO}_2$ ,  $\text{CH}_4$  and  $\text{N}_2$  gases by using concentration pulse chromatography method (CPM) (see supplemental material for details pertaining to this method). These values are displayed in Table 5 for different temperatures. Henry's Law constants are related directly to the shape of adsorption isotherms at low pressures. Adsorption isotherms of  $\text{CO}_2$  on all clinoptilolite types and at all temperatures have the highest slope in the low pressure region. The  $K_p$  values are the highest for  $\text{CO}_2$ . They show the following trend for  $\text{CO}_2$ :  $\text{Fe}^{3+} < \text{Cs}^+ < \text{Ca}^{2+} < \text{Raw}$ . These higher values are indicate a high level of interaction between the  $\text{CO}_2$  adsorbate molecules and the surface as discussed in Section 4.1.

As can be seen in Table 5, both  $\text{CH}_4$  and  $\text{N}_2$  show significantly weaker interaction with all of the adsorbents compared to  $\text{CO}_2$ . The  $K_p$  values determined using the CPM are low for  $\text{CH}_4$  and  $\text{N}_2$ . The range of  $K_p$  values are fairly similar for both gases, with  $\text{CH}_4$  being slightly higher than  $\text{N}_2$  for  $\text{Fe}^{3+}$ , and  $\text{Cs}^+$  clinoptilolite, are similar for raw clinoptilolite and are lower for  $\text{Ca}^{2+}$  clinoptilolite. It is evident that there is likely reduced interaction for both of the  $\text{N}_2$  and  $\text{CH}_4$  since the Henry's Law constant values are lower compared to  $\text{CH}_4$ . This can be a consequence of the steric effects resulting from restricted micropore access for these gases. Fig. 7 presents the van't Hoff plots for the Henry's Law constants measured for  $\text{CO}_2$ ,  $\text{CH}_4$ , and  $\text{N}_2$  for the studied adsorbents. As can be seen in Fig. 7, the slope of the van't Hoff plots are fairly flat for the  $\text{CH}_4$  and  $\text{N}_2$  gases compared to  $\text{CO}_2$ . This trend may be explained by the influence of microporous diffusion resistance in the micropores of this zeolite. The chromatographic method is a dynamic method because the flow rate of the He carrier gas influences the exposure of the gas molecules to the micropores of the adsorbent. Microporous diffusion limitations would manifest itself with lower observed  $K_p$  values, which is indicative of less interaction between the gas and the adsorbent. For example,  $\text{Ca}^{2+}$  clinoptilolite (which is known to have smaller effective micropore size and slower diffusion rates [59])

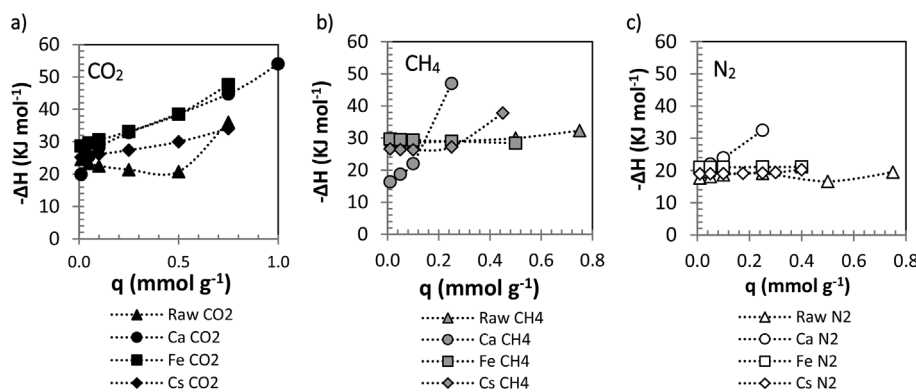


**Fig. 8.** Isosteric heat of adsorption values for a)  $\text{CO}_2$ , b)  $\text{CH}_4$ , and c)  $\text{N}_2$  for raw clinoptilolite compared to  $\text{Fe}^{3+}$ ,  $\text{Ca}^{2+}$ , and  $\text{Cs}^+$  exchanged clinoptilolite. The best temperature dependent adsorption model fit was used, which was determined from the lowest sum of the squared residuals between the experimental and predicted adsorption capacities. The dash lines are a guide to the eye.

**Table 7**

Experimental isosteric heat of adsorption at near zero coverage calculated from the adsorption equilibria data and comparison with literature.

Adsorbent	$-\Delta H \text{ (kJ mol}^{-1})$			Ref.
	$\text{CO}_2$	$\text{CH}_4$	$\text{N}_2$	
Raw Clinoptilolite	24.5	28.4	17.6	Current Study
$\text{Ca}^{2+}$ Clinoptilolite	19.9	16.3	20.7	
$\text{Cs}^+$ Clinoptilolite	25.2	26.6	18.9	
$\text{Fe}^{3+}$ Clinoptilolite	28.6	29.7	20.9	
natural Clinoptilolite	42.3	–	24.9	[91]
natural Clinoptilolite	21.0	11.62	–	[84]

shows the smallest  $K_p$  values for  $\text{CH}_4$  thus indicating less interaction between the large  $\text{CH}_4$  molecule and the small micropores of the adsorbent. On the other hand, the  $\text{Fe}^{3+}$  clinoptilolite (which has much lower microporous diffusion resistance [81]) exhibits higher  $K_p$  values and a greater slope than  $\text{Ca}^{2+}$  clinoptilolite. While great care is given to ensure that the CPM experimental conditions were optimal (carrier gas flow rate, temperature, sample gas injection volume etc.) the microporous diffusional limitation inherent with this material makes it difficult achieve reliable results with this method. CPM also has its limitations as a method to measure adsorption characteristics. If the Henry's Law constants and the diffusivities are very low, it is impossible to measure the Henry's Law constants accurately due to the assumptions

### $\text{CO}_2/\text{CH}_4$

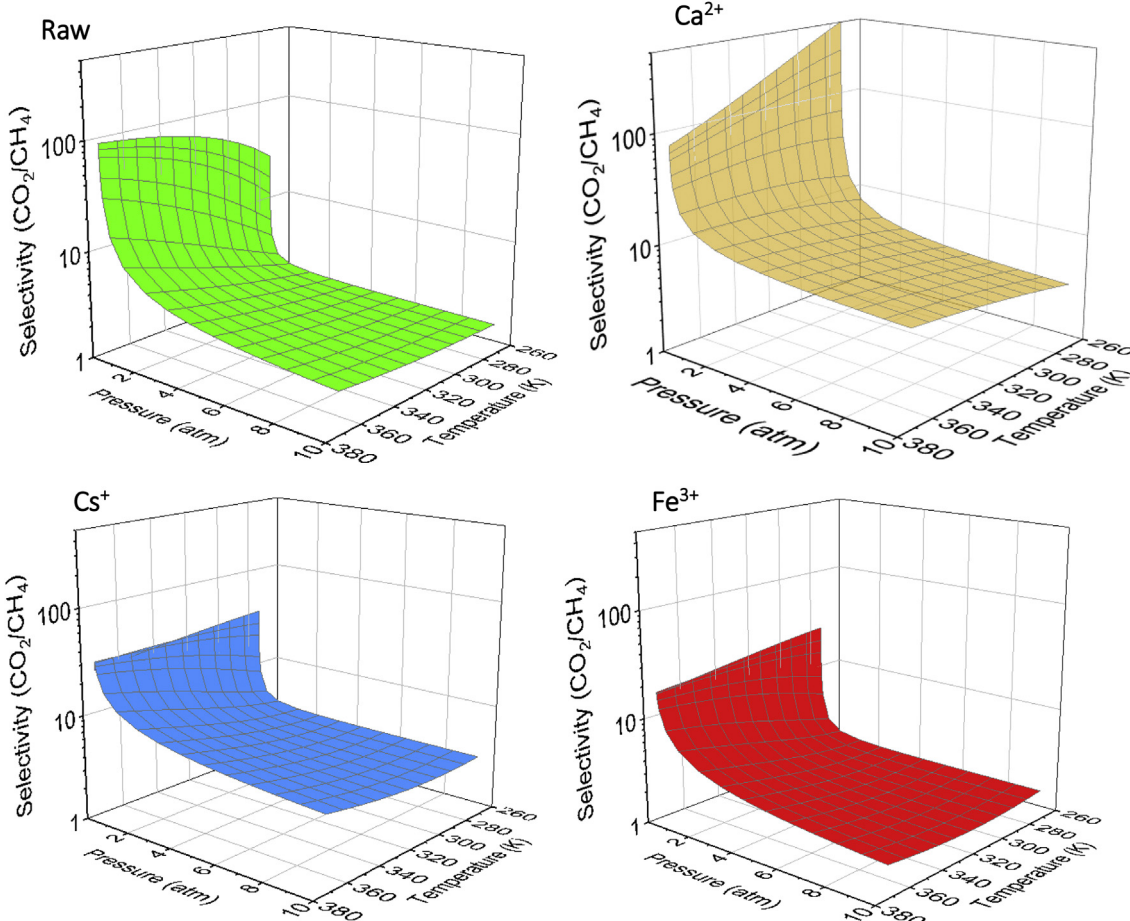


**Fig. 9.** Predicted  $\text{CO}_2/\text{CH}_4$  ideal selectivity for raw clinoptilolite compared to  $\text{Fe}^{3+}$ ,  $\text{Ca}^{2+}$ , and  $\text{Cs}^+$  exchanged clinoptilolite over a temperature range of 273 K–373 K and pressure range of 0.001 atm–10 atm.

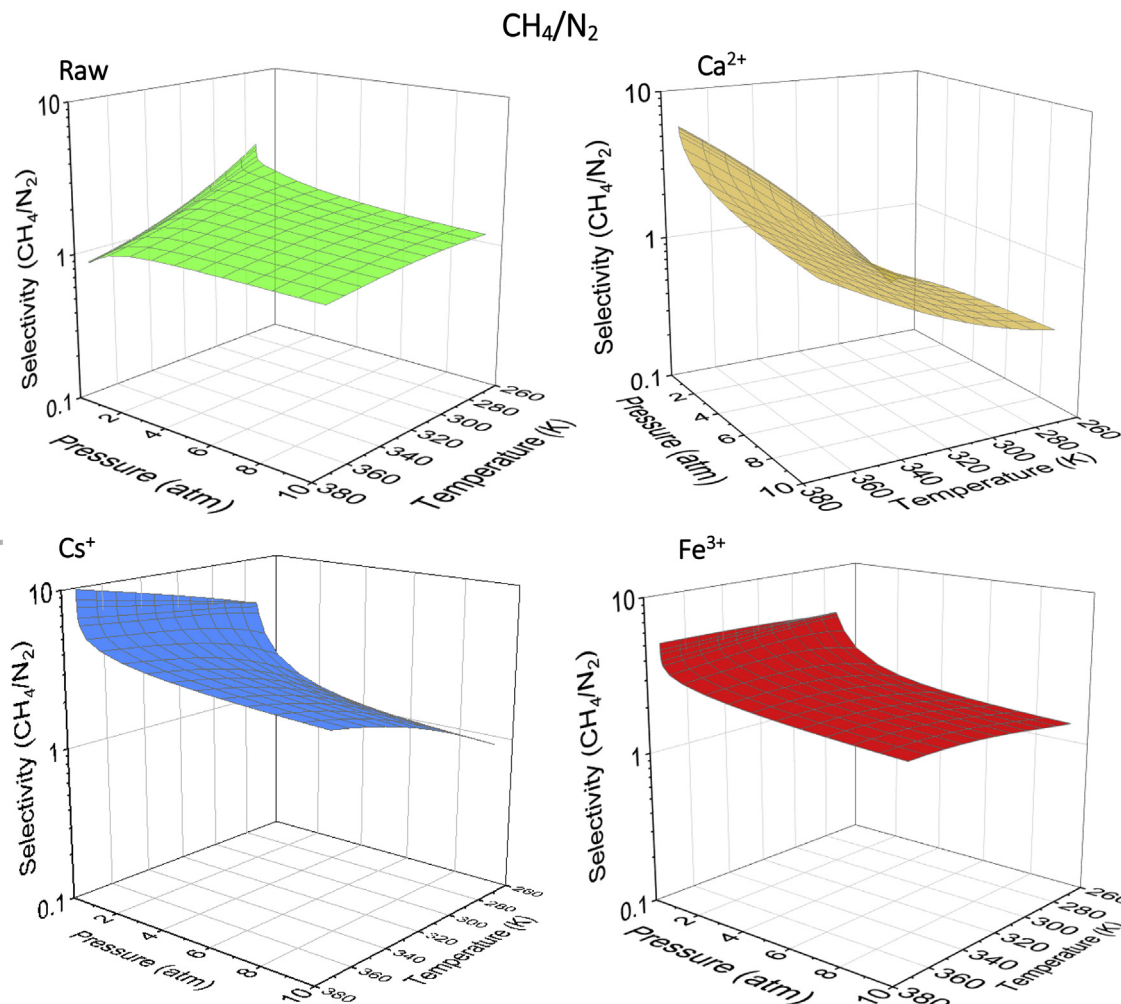


**Fig. 10.** Predicted  $\text{CH}_4/\text{N}_2$  ideal selectivity for raw clinoptilolite compared to  $\text{Fe}^{3+}$ ,  $\text{Ca}^{2+}$ , and  $\text{Cs}^+$  exchanged clinoptilolite over a temperature range of 273 K–373 K and pressure range of 0.001 atm–10 atm.

made for the equations used for the calculations.

Table 6 shows the calculated limiting heat of adsorption values determined from the CPM technique according to the van't Hoff equation (Equation (9)) using the  $K_p$  values determined. While the heat of adsorption values for  $\text{CO}_2$  are similar, they are far lower than the accepted literature values for  $\text{CH}_4$  and  $\text{N}_2$  on raw clinoptilolite [84,91]. Given this discrepancy, and the questionable use of CPM for very low  $K_p$  values as explained in the above paragraph, the heat of adsorption values were also estimated from the experimental isotherm data obtained at different temperatures (Figs. 3–5) using the Clausius-Clapeyron equation (Equation (10)). Adsorption is an exothermic process. Therefore increasing the temperature will decrease the adsorbate-adsorbent interaction and lower the adsorption capacity. The effect of adsorbate surface loading on the thermodynamic tendencies presents itself as the isosteric heat of adsorption which is presented in Fig. 8. The isosteric heat of adsorption values at near zero coverage are determined using the y-axis intercept of this figure and are presented in Table 7. The isosteric heats of adsorption calculated for all of the clinoptilolite types at low loadings are in the order of  $\text{N}_2 < \text{CH}_4 < \text{CO}_2$ . Comparing these values with literature, the isosteric heat of adsorption values differ only slightly than the values found for raw clinoptilolite [84,91]. The differences are likely due to the variations in clinoptilolite composition which depends on the local mineral source.

Considering only the heat of adsorption values for  $\text{CO}_2$ ; both  $\text{Fe}^{3+}$  and  $\text{Ca}^{2+}$  clinoptilolite have the highest isosteric heat of adsorption at higher loadings (see Fig. 8).  $\text{CO}_2$  interactions with these adsorbents are

concentrated towards the highly charged cationic sites meaning that adsorbate - adsorbent interactions have the strongest temperature dependence due to the close proximity of the adsorbed gases. The isosteric heat for  $\text{CO}_2$  increases as loading increase, these interactions dominate as loading increases for all of the clinoptilolite types. This trend is the most pronounced on the  $\text{Ca}^{2+}$  clinoptilolite, and is actually observable for all three gases. This makes sense given that intermolecular interactions are expected to increase when the effective pore size is more restricted.

#### 4.3. Separation predictions of $\text{CO}_2$ and $\text{N}_2$ from $\text{CH}_4$ (ideal selectivity)

Figs. 9 and 10 present the ideal equilibrium adsorption selectivity for  $\text{CO}_2/\text{CH}_4$  and  $\text{CH}_4/\text{N}_2$ , respectively, on the different clinoptilolite types which were calculated using Equation (12) from the pure component adsorption data. The best isotherm model was chosen for the regression of the experimental values as described in Section 4.1 using the selected parameters given in Table 2. The temperature and pressure bounds, which were between 273 and 373 K and 0.001–10 atm, respectively, were chosen to display the selectivity with reasonable confidence. However, caution should be taken when using the single gas isotherm regressions to extrapolate to full scale adsorption systems. This is due to the inherent limitations of this approach as it assume ideal behaviour and it discounts the effects of kinetic behaviour or competitive adsorption which is present in adsorbing gas mixtures such as in this system [51,99,124–126]. Nonetheless, the ideal selectivity

values provide a basic initial assessment for identifying the best criteria for augmenting the separation performance of these materials [54]. Subsequent adsorption mixture analysis would be necessary to properly assess the potential of these materials for these gas separations.

The ideal selectivity changes dramatically depending on the type of cation exchanged which confirms the findings as discussed in our previous study for  $\text{Ca}^{2+}$ ,  $\text{Cs}^+$ , and  $\text{Fe}^{3+}$  cation exchanged clinoptilolite [81]. As shown in Fig. 9, the  $\text{CO}_2/\text{CH}_4$  ideal selectivity increases with decreasing pressure for all of the clinoptilolite types and is the greatest at pressures below 1 atm. This is the result of the more rectangular shape of the  $\text{CO}_2$  isotherms as can be seen in Fig. 3, compared to the ones for  $\text{CH}_4$  in Fig. 4.  $\text{Ca}^{2+}$  clinoptilolite has the highest  $\text{CO}_2/\text{CH}_4$  selectivity among all of the clinoptilolite types and is over 300 at 273 K and 0.001 atm. Above 1 atm, the temperature and pressure effects on the ideal  $\text{CO}_2/\text{CH}_4$  selectivity are less dramatic and the selectivity value change from about 4.5 at 273 K and 10 atm to 25 at 373 K and 1 atm for  $\text{Ca}^{2+}$  clinoptilolite.

It is generally accepted in the literature that  $\text{Ca}^{2+}$  clinoptilolite shows high microporous diffusion resistance [69,81,90]. However, at higher temperatures this effect is minimized as shown in Fig. 6. Therefore, while adsorbent capacity decreases with increasing temperature; greater ideal selectivity and faster adsorption kinetics may compensate for this behaviour at higher temperatures. This is also apparent for the  $\text{CH}_4/\text{N}_2$  ideal selectivity on the  $\text{Ca}^{2+}$  clinoptilolite which shows the greatest sensitivity to temperature and pressure for this separation. As shown in Fig. 10, the  $\text{CH}_4/\text{N}_2$  ideal selectivity ranges from 0.3 ( $\text{N}_2/\text{CH}_4$  selective) at 273 K and 0.001 atm up to 5.5 at 373 K and 0.001 atm for this adsorbent. Both  $\text{Cs}^+$  and  $\text{Fe}^{3+}$  clinoptilolite show higher  $\text{CH}_4/\text{N}_2$  ideal selectivity values compared to the raw clinoptilolite that has values close to unity for this separation. The  $\text{CH}_4/\text{N}_2$  ideal selectivity approaches unity for  $\text{Cs}^+$  clinoptilolite at 273 K and 10 atm and increases to 10 at 373 K and 0.001 atm, and generally increases with increasing temperature and decreasing pressure. In comparison,  $\text{Fe}^{3+}$  clinoptilolite has  $\text{CH}_4/\text{N}_2$  separation values which are less sensitive and range from 3 to 6 across the range of temperatures and pressures studied.

## 5. Conclusions

The effect of temperature on the adsorption characteristics of  $\text{CO}_2$ ,  $\text{CH}_4$ , and  $\text{N}_2$  gases was studied on raw and cation exchanged clinoptilolite with  $\text{Ca}^{2+}$ ,  $\text{Fe}^{3+}$ , and  $\text{Cs}^+$  cations. Temperature dependent isotherm models were curve fitted with experimental data to determine the best model to represent the data. Selectivity factor values were calculated for  $\text{CO}_2/\text{CH}_4$  and  $\text{CH}_4/\text{N}_2$  gas separation applications using the regressed isotherm models that had the best representation of the experimental data. The  $\text{CH}_4$  and  $\text{N}_2$  adsorption kinetics were determined and compared for raw and  $\text{Ca}^{2+}$  clinoptilolite. These results showed higher microporous diffusion resistance for  $\text{Ca}^{2+}$  clinoptilolite for both gases which dissipates with increasing temperatures. The isosteric heat of adsorption value was the highest for  $\text{CO}_2$  followed by  $\text{CH}_4$ , and  $\text{N}_2$ , and was shown to increase with the amount of surface coverage for clinoptilolite types for  $\text{CO}_2$ , and all three gases for  $\text{Ca}^{2+}$  clinoptilolite. Among the different types of clinoptilolites,  $\text{Ca}^{2+}$  clinoptilolite shows the best potential for  $\text{CO}_2/\text{CH}_4$  separations due to its higher selectivity. However, it is recommended that higher adsorption temperatures be used for this adsorbent in order to compensate for the slow kinetic behaviour at low temperatures. For  $\text{CH}_4/\text{N}_2$  separations, Both  $\text{Cs}^+$  and  $\text{Fe}^{3+}$  display higher selectivity values compared to the raw clinoptilolite which had values close to unity. However, the  $\text{Fe}^{3+}$  clinoptilolite selectivity displays less variability which means that it would be most effective over a broader range of temperatures and pressures for this separation. The selectivity plots serve only as a guide to define suitable operating ranges for the materials. However, further study is necessary to determine the true performance of these materials using mixture adsorption analysis.

## Nomenclature

$B$	adsorption affinity constant [ $\text{atm}^{-1}$ ]
$B_0$	adsorption affinity constant at reference temperature [ $\text{atm}^{-1}$ ]
$D_e$	effective (transport) diffusivity [ $\text{m}^2/\text{s}$ ]
$D_e/R_p^2$	diffusion time constant [ $\text{s}^{-1}$ ]
$\Delta H$	limiting heat of adsorption [ $\text{kJ/mol}$ ]
$k_1$	TD - DS Langmuir parameter [ $\text{mmol/g}$ ]
$k_2$	TD - DS Langmuir parameter [ $\text{mmol/g K}$ ]
$k_3$	TD - DS Langmuir parameter [ $\text{atm}^{-1}$ ]
$k_4$	TD - DS Langmuir parameter [K]
$K$	dimensionless Henry's Law constant [dimensionless]
$K_p$	dimensional Henry's Law constant [ $\text{mmol/g atm}$ ]
$k_{\text{LDF}}$	LDF model kinetic rate constant [ $\text{s}^{-1}$ ]
$L$	length of the column [m]
$n$	dimensionless model parameter [dless]
$n_0$	dimensionless model parameter at reference temperature [dless]
$P$	pressure [atm]
$P_0$	saturation pressure [atm]
$q$	amount adsorbed [ $\text{mmol/g}$ of adsorbent]
$q(t)$	amount absorbed at time $t$ [ $\text{mmol/g}$ of adsorbent]
$q_e$	adsorption capacity at equilibrium [ $\text{mmol/g}$ of adsorbent]
$q_m$	adsorption capacity at saturation [ $\text{mmol/g}$ of adsorbent]
$q_{m0}$	adsorption capacity at reference temperature [ $\text{mmol/g}$ of adsorbent]
$Q$	heat of adsorption model parameter [ $\text{kJ/mol}$ ]
$R$	universal gas constant [ $\text{m}^3 \text{Pa/K mol}$ ]
$R_p$	radius of particle [m]
$t$	time [s]
$T$	temperature [K]

### Subscripts

1	component 1
2	component 2
A	adsorption site A
B	adsorption site B

### Greek Symbols

$\alpha_{1/2}$	apparent adsorption equilibrium selectivity factor, [dimensionless]
$\alpha_n$	dimensionless model parameter at reference temperature [dimensionless]
$\beta$	kinetic selectivity factor [dimensionless]
$\epsilon$	bed porosity [dimensionless]
$\theta$	adsorption surface coverage [dimensionless]
$\chi$	dimensionless model parameter at reference temperature [dimensionless]
$\mu$	mean retention time [s]
$\mu_D$	system dead time [s]
$v$	Interstitial velocity [cm/s]
$\rho_p$	adsorbent pellet density [g/cm <sup>3</sup> ]

### Abbreviations

BET	Brunauer – Emmett – Teller
CMS	carbon molecular sieve
CPM	concentration pulse method
DS	dual site
EDS	electron dispersive spectroscopy
ETS-4	Engelhard Titanosilicate 4
FD	Fickian Diffusion model
GC	gas chromatograph
HEU	Heulandite
HK	Horvath-Kawazoe
LDF	linear driving force

MOF	metal organic framework
PSA	pressure swing adsorption
SSR	sum of the squared residuals
TCD	Thermal conductivity detector
TD	Temperature dependent
VPSA	vacuum pressure swing adsorption
VSA	vacuum swing adsorption

## Appendix A. Supplementary data

Supplementary data related to this article can be found at <https://doi.org/10.1016/j.micromeso.2018.08.035>.

## References

- [1] International Energy Agency, Key World Energy Statistics 2015, Paris, (2015).
- [2] International Energy Agency, Energy and Climate Change: World Energy Outlook Special Report, (2015).
- [3] M. Tagliabue, D. Farrusseng, S. Valencia, S. Aguado, U. Ravon, C. Rizzo, A. Corma, C. Mirodatos, Chem. Eng. J. 155 (2009) 553–566.
- [4] A. Kidnay, W. Parrish, D. McCartney, Fundamentals of Natural Gas Processing, second ed., CRC Press, 2011.
- [5] T.E. Rufford, S. Smart, G.C.Y. Watson, B.F. Graham, J. Boxall, J.C. Diniz da Costa, E.F. May, J. Petrol. Sci. Eng. 94–95 (2012) 123–154.
- [6] F.C. Seeger, Method and System for Enhancing Natural Gas Production, WO2015178898 A1 (2015).
- [7] T.L. Saleman, G. Li, T.E. Rufford, P.L. Stanwix, K.I. Chan, S.H. Huang, E.F. May, Chem. Eng. J. 281 (2015) 739–748.
- [8] H.R. Sant Anna, A.G. Barreto, F.W. Tavares, J.F. do Nascimento, Chem. Eng. Process. Process Intensif. 103 (2016) 70–79.
- [9] S. Cavenati, C.A. Grande, A.E. Rodrigues, J. Chem. Eng. Data 49 (2004) 1095–1101.
- [10] V.P. Mulgundmath, F.H. Tezel, T. Saatcioglu, T.C. Golden, Can. J. Chem. Eng. 90 (2012) 730–738.
- [11] J. Zhang, R. Singh, P.A. Webley, Microporous Mesoporous Mater. 111 (2008) 478–487.
- [12] P. Li, F.H. Tezel, J. Chem. Eng. Data 53 (2008) 2479–2487.
- [13] X. Liu, J. Li, L. Zhou, D. Huang, Y. Zhou, Chem. Phys. Lett. 415 (2005) 198–201.
- [14] R. Hernández-Huesca, L. Díaz, G. Aguilar-Armenta, Separ. Purif. Technol. 15 (1999) 163–173.
- [15] T.C. Golden, S. Sircar, J. Colloid Interface Sci. 162 (1994) 182–188.
- [16] S.-T. Yang, J. Kim, W.-S. Ahn, Microporous Mesoporous Mater. 135 (2010) 90–94.
- [17] J.A. Delgado, M.A. Uguina, J.L. Sotelo, B. Ruiz, M. Rosario, J. Nat. Gas Chem. 16 (2007) 235–243.
- [18] E. García-Pérez, J.B. Parra, C.O. Ania, A. García-Sánchez, J.M. van Baten, R. Krishna, D. Dubbeldam, S. Calero, Adsorption 13 (2007) 469–476.
- [19] F. Dreisbach, R. Staudt, J.U. Keller, Adsorption 5 (1999) 215–227.
- [20] S. Himeno, T. Komatsu, S. Fujita, J. Chem. Eng. Data 50 (2005) 369–376.
- [21] M. Nandi, K. Okada, A. Dutta, A. Bhaumik, J. Maruyama, D. Derk, H. Uyama, M. Asta, B.W. Laird, O.M. Yaghi, Chem. Commun. 48 (2012) 10283.
- [22] X. Shao, Z. Feng, R. Xue, C. Ma, W. Wang, X. Peng, D. Cao, AIChE J. 57 (2011) 3042–3051.
- [23] M.S. Shafeeyan, W.M.A.W. Daud, A. Houshmand, A. Shamiri, J. Anal. Appl. Pyrolysis 89 (2010) 143–151.
- [24] P. Halder, M. Maurya, S.K. Jain, J.K. Singh, X. Lu, S. Jiang, W. Shen, M. Yumura, S. Iijima, S. Iijima, G.E. Scuseria, D. Tomaneck, J.E. Fisher, R.E. Smalley, Phys. Chem. Chem. Phys. 18 (2016) 14007–14016.
- [25] X. Peng, W. Wang, R. Xue, Z. Shen, AIChE J. 52 (2006) 994–1003.
- [26] A. Kapoor, R.T. Yang, Chem. Eng. Sci. 44 (1989) 1723–1733.
- [27] Y.-S. Bae, K.L. Mulfort, H. Frost, P. Ryan, S. Punnathanam, L.J. Broadbelt, J.T. Hupp, R.Q. Snurr, Langmuir 24 (2008) 8592–8598.
- [28] D. Saha, Z. Bao, F. Jia, S. Deng, Environ. Sci. Technol. 44 (2010) 1820–1826.
- [29] L. Hamon, E. Jolimaitre, G.D. Pirngruber, Ind. Eng. Chem. Res. 49 (2010) 7497–7503.
- [30] L. Hamon, P.L. Llewellyn, T. Devic, A. Ghoufi, G. Clet, V. Guillerm, G.D. Pirngruber, G. Maurin, C. Serre, G. Driver, W. van Beek, E. Jolimaitre, A. Vimont, M. Daturi, G. Férey, J. Am. Chem. Soc. 131 (2009) 17490–17499.
- [31] L. Bastin, P.S. Bárcia, E.J. Hurtado, J.A.C. Silva, A.E. Rodrigues, C. Banglin, (2008).
- [32] R. Zhong, Z. Xu, W. Bi, S. Han, X. Yu, R. Zou, Inorg. Chim. Acta. 443 (2016) 299–303.
- [33] J.-R. Li, R.J. Kuppler, H.-C. Zhou, Chem. Soc. Rev. 38 (2009) 1477.
- [34] J. Pérez-Pellitero, H. Amrouche, F.R. Siperstein, G. Pirngruber, C. Nieto-Draghi, G. Chaplais, A. Simon-Masseron, D. Bazer-Bachi, D. Peralta, N. Bats, Chem. Eur. J. 16 (2010) 1560–1571.
- [35] Y. Belmabkhout, G. De Weireld, A. Sayari, Langmuir 25 (2009) 13275–13278.
- [36] C. Gunathilake, M. Gangoda, M. Jaroniec, Ind. Eng. Chem. Res. 55 (2016) 5598–5607.
- [37] Y. Belmabkhout, A. Sayari, Adsorption 15 (2009) 318–328.
- [38] P.J.E.H. and, A. Sayari\*, (2006).
- [39] S. Couck, J.F.M. Denayer, G.V. Baron, T. Rémy, J. Gascon, F. Kapteijn, J. Am. Chem. Soc. 131 (2009) 6326–6327.
- [40] A. Sayari, A. Heydari-Gorji, Y. Yang, J. Am. Chem. Soc. 134 (2012) 13834–13842.
- [41] F. Rezaei, C.W. Jones, Ind. Eng. Chem. Res. 53 (2014) 12103–12110.
- [42] A. Heydari-Gorji, A. Sayari, Ind. Eng. Chem. Res. 51 (2012) 6887–6894.
- [43] D. Ma, Y. Li, Z. Li, Chem. Commun. 47 (2011) 7377.
- [44] J.A. Greathouse, M.D. Allendorf, J. Am. Chem. Soc. 128 (2006) 10678–10679.
- [45] Long Pan, Brett Parker, Xiaoying Huang, David H. Olson, and JeongYong Lee, J. Li\*, (2006).
- [46] N.C. Burtch, H. Jasuja, K.S. Walton, Chem. Rev. 114 (2014) 10575–10612.
- [47] J. Canivet, A. Fateeva, Y. Guo, B. Coasne, D. Farrusseng, Chem. Soc. Rev. 43 (2014) 5594–5617.
- [48] K.S. Park, Z. Ni, A.P. Côté, J.Y. Choi, R. Huang, F.J. Uribe-Romo, H.K. Chae, M. O'Keefe, O.M. Yaghi, Proc. Natl. Acad. Sci. U.S.A. 103 (2006) 10186–10191.
- [49] M. Kacem, M. Pellerano, A. Delebarre, Fuel Process. Technol. 138 (2015) 271–283.
- [50] Y.J. Wu, Y. Yang, X.M. Kong, P. Li, J.G. Yu, A.M. Ribeiro, A.E. Rodrigues, J. Chem. Eng. Data 60 (2015) 2684–2693.
- [51] D.A. Kennedy, M. Mujcin, E. Trudeau, F.H. Tezel, J. Chem. Eng. Data 61 (2016) 3163–3176.
- [52] A. Bakhtyari, M. Mofarahi, J. Chem. Eng. Data 59 (2014) 626–639.
- [53] M. Mofarahi, A. Bakhtyari, J. Chem. Eng. Data 60 (2015) 683–696.
- [54] N.K. Jensen, T.E. Rufford, G. Watson, D.K. Zhang, K.I. Chan, E.F. May, J. Chem. Eng. Data 57 (2012) 106–113.
- [55] J. Shang, G. Li, Q. Gu, R. Singh, P. Xiao, J.Z. Liu, P.A. Webley, C.M. Doherty, A.J. Hill, J.Z. Liu, P.A. Webley, Chem. Commun. 50 (2014) 4544–4545.
- [56] J.A. Delgado, M.A. Uguina, J.M. Gómez, L. Ortega, Separ. Purif. Technol. 48 (2006) 223–228.
- [57] M.W. Ackley, R.T. Yang, AIChE J. 37 (1991) 1645–1656.
- [58] A. Jayaraman, A.J. Hernandez-Maldonado, R.T. Yang, D. Chinn, C.L. Munson, D.H. Mohr, Chem. Eng. Sci. 59 (2004) 2407–2417.
- [59] M.W. Ackley, R.F. Giese, R.T. Yang, Zeolites 12 (1992) 780–788.
- [60] S. Cavenati, C.A. Grande, A.E. Rodrigues, Chem. Eng. Sci. 61 (2006) 3893–3906.
- [61] Y. Gogotsi, A. Nikitin, H. Ye, W. Zhou, J.E. Fischer, B. Yi, H.C. Foley, M.W. Barsoum, Nat. Mater. 2 (2003) 591–594.
- [62] S. Cavenati, C.A. Grande, A.E. Rodrigues, Adsorption 11 (2005) 549–554.
- [63] J.W. Yoon, H. Chang, S.-J. Lee, Y.K. Hwang, D.-Y. Hong, S.-K. Lee, J.S. Lee, S. Jang, T.-U. Yoon, K. Kwac, Y. Jung, R.S. Pillai, F. Faucher, A. Vimont, M. Daturi, G. Férey, C. Serre, G. Maurin, Y.-S. Bae, J.-S. Chang, Nat. Mater. 16 (2017) 526–531.
- [64] S.M. Kuznicki, V.A. Bell, S. Nair, H.W. Hillhouse, R.M. Jacubinas, C.M. Braunbarth, B.H. Toby, M. Tsapatsis, Nature 412 (2001) 720–724.
- [65] C. Baerlocher, L.B. McCusker, Database of Zeolite Structures, Structural Commission of the International Zeolite Association, 2017.
- [66] K. Koyama, Y. Takéuchi, Zeitschrift Fur Krist. - New Cryst. Struct. 145 (1977) 216–239.
- [67] N. Mansouri, N. Rikhtegar, H.A. Panahi, F. Atabi, B.K. Shahrai, Environ. Protect. Eng. 39 (2013) 139–152.
- [68] M.W. Ackley, R.T. Yang, Ind. Eng. Chem. Res. 30 (1991) 2523–2530.
- [69] M.W. Ackley, R.F. Giese, R.T. Yang, Zeolites 12 (1992) 780–788.
- [70] M.A. Hernández, F. Rojas, V.H. Lara, J. Porous Mater. 7 (2000) 443–454.
- [71] M. Johnson, D. O'Connor, P. Barnes, C.R.A. Catlow, S.L. Owens, G. Sankar, R. Bell, S.J. Teat, R. Stephenson, J. Phys. Chem. B 107 (2003) 942–951.
- [72] T. Armbruster, Am. Mineral. 78 (1993) 260–264.
- [73] K. Koyama, Y. Takeuchi, Z. für Kristallogr. - Cryst. Mater. 145 (1977).
- [74] Y. Garcia-Basabe, A.R. Ruiz-Salvador, G. Maurin, L.-C. de Menorval, I. Rodriguez-Izaga, A. Gomez, Microporous Mesoporous Mater. 155 (2012) 233–239.
- [75] L.T. Dimowa, O.E. Petrov, N.I. Djourelow, B.L. Shivachev, Clay Miner. 50 (2015).
- [76] E.L. Uzonova, H. Mikosch, Microporous Mesoporous Mater. 177 (2013) 113–119.
- [77] M.W. Ackley, R.T. Yang, Ind. Eng. Chem. Res. 30 (1991) 2523–2530.
- [78] G. Aguilar-Armenta, G. Hernandez-Ramirez, E. Flores-Loyola, A. Ugarte-Castaneda, R. Silva-Gonzalez, C. Tabares-Munoz, A. Jimenez-Lopez, E. Rodriguez-Castellon, J. Phys. Chem. B 105 (2001) 1313–1319.
- [79] T.C. Frankiwicz, R.G. Donnelly, Methane/nitrogen Gas Separation over the Zeolite Clinoptilolite by the Selective Adsorption of Nitrogen, American Chemical Society, 1983.
- [80] D.A. Kennedy, F.H. Tezel, Microporous Mesoporous Mater. 262 (2018) 235–250.
- [81] L. Predescu, F.H. Tezel, Stud. Surf. Sci. Catal. 97 (1995) 507–512.
- [82] G. Aguilar-Armenta, G. Hernandez-Ramirez, E. Flores-Loyola, A. Ugarte-Castaneda, R. Silva-Gonzalez, C. Tabares-Munoz, A. Jimenez-Lopez, E. Rodriguez-Castellon, J. Phys. Chem. B 105 (2001) 1313–1319.
- [83] A. Arefi Pour, S. Sharifnia, R. NeishaboriSalehi, M. Ghodrati, J. Nat. Gas Sci. Eng. 26 (2015) 1246–1253.
- [84] A. Jayaraman, A.J. Hernandez-Maldonado, R.T. Yang, D. Chinn, C.L. Munson, D.H. Mohr, Chem. Eng. Sci. 59 (2004) 2407–2417.
- [85] A. Jayaraman, R.T. Yang, D. Chinn, C.L. Munson, Ind. Eng. Chem. Res. 44 (2005) 5184–5192.
- [86] B.E. Alver, M. Sakizci, Adsorption 21 (2015) 391–399.
- [87] R.W. Tribe, F.H. Tezel, Gas Separ. Purif. 9 (1995) 223–230.
- [88] G. Aguilar-Armenta, M.E. Patiño-Iglesias, R.L.-R. Centro, 2 (2002) 81–91.
- [89] E. Kouvelos, K. Kesore, T. Steriotis, H. Grigoropoulou, D. Bouloubasi, N. Theophilou, S. Tzintzos, N. Kanelopoulos, Microporous Mesoporous Mater. 99 (2007) 106–111.
- [90] D.S. Karousos, A.A. Sapalidis, E.P. Kouvelos, G.E. Romanos, N.K. Kanellopoulos, Separ. Sci. Technol. 51 (2016) 83–95.
- [91] S. Brunauer, L.S. Deming, W.E. Deming, E. Teller, J. Am. Chem. Soc. 62 (1940) 1723–1732.
- [92] S.U. Rege, R.T. Yang, AIChE J. 46 (2000) 734–750.

- [94] G. Horváth, K. Kawazoe, *J. Chem. Eng. Jpn.* 16 (1983) 470–475.
- [95] D.M. Ruthven, *Principles of Adsorption and Adsorption Processes*, John Wiley & Sons, Toronto, 1984.
- [96] I. Langmuir, *J. Am. Chem. Soc.* 40 (1918) 1361–1403.
- [97] R. Sips, *J. Chem. Phys.* 16 (1948) 490–495.
- [98] A.L. Myers, *AIChE J.* 29 (1983) 691–693.
- [99] P. Li, F. Tezel, *J. Chem. Eng. Data* 54 (2009) 8–15.
- [100] D.M. Ruthven, *Mol. Sieves - Sci. Technol.* 7 (2008) 1–43.
- [101] D.D. Do, *Adsorption Analysis: Equilibria and Kinetics*, Imperial College Press, London, 1998.
- [102] E.S. Kikkilides, R.T. Yang, S.H. Cho, *Ind. Eng. Chem. Res.* 32 (1993) 2714–2720.
- [103] D.M. Ruthven, R. Kumar, *Ind. Eng. Chem. Fundam.* 19 (1980) 27–32.
- [104] S.H. Hyun, R.P. Danner, *J. Chem. Eng. Data* 27 (1982) 196–200.
- [105] S.H. Hyun, R.P. Danner, *AIChE J.* 31 (1985) 1077–1085.
- [106] F.H. Tezel, H. Tezel, D.M. Ruthven, *J. Colloid Interface Sci.* 149 (1992) 197–207.
- [107] R. Yang, *Gas Separation by Adsorption Processes*, Butterworth Publishers, Toronto, 1987.
- [108] P.H. Nelson, S.M. Auerbach, *J. Chem. Phys.* 110 (1999) 9235.
- [109] S. Sircar, J.R. Hutton, *Adsorption* 6 (2000) 137–147.
- [110] E. Glueckauf, *Trans. Faraday Soc.* 51 (1955) 1540.
- [111] E. Glueckauf, J.I. Coates, *J. Chem. Soc.* (1947) 1315.
- [112] C.R. Reid, K.M. Thomas, *Langmuir* 15 (1999) 3206–3218.
- [113] M.W. Ackley, R.F. Giese, R.T. Yang, *Zeolites* 12 (1992) 780–788.
- [114] J. Zhang, R. Singh, P.A. Webley, *Microporous Mesoporous Mater.* 111 (2008) 478–487.
- [115] S. Sircar, *Ind. Eng. Chem. Res.* 45 (2006) 5435–5448.
- [116] R.D. Shannon, *IUCr, Acta Crystallogr. Sect. A* 32 (1976) 751–767.
- [117] J.C. Slater, *J. Chem. Phys.* 41 (1964) 3199–3204.
- [118] T.D. Pham, Q. Liu, R.F. Lobo, *Langmuir* 29 (2013) 832–839.
- [119] K.S. Walton, M.B. Abney, M. Douglas LeVan, *Microporous Mesoporous Mater.* 91 (2006) 78–84.
- [120] M. Huang, S. Kaliaguine, *J. Chem. Soc. Faraday Trans.* 88 (1992) 751.
- [121] P. Castaldi, L. Santona, C. Cozza, V. Giuliano, C. Abbruzzese, V. Nastro, P. Melis, *J. Mol. Struct.* 734 (2005) 99–105.
- [122] M.K. Doula, *Chemosphere* 67 (2007) 731–740.
- [123] Y. Yokomichi, T. Yamabe, T. Kakimoto, O. Okada, H. Ishikawa, Y. Nakamura, H. Kimura, I. Yasuda, *Appl. Catal. B Environ.* 28 (2000) 1–12.
- [124] M. Mofarahi, A. Bakhtyari, *J. Chem. Eng. Data* 60 (2015) 683–696.
- [125] P.J.E. Harlick, F.H. Tezel, *Separ. Sci. Technol.* 37 (2002) 33–60.
- [126] Y.-J. Wu, Y. Yang, X.-M. Kong, P. Li, J.-G. Yu, A.M. Ribeiro, A.E. Rodrigues, *J. Chem. Eng. Data* 60 (2015) 2684–2693.